Wireless Wearable Sensor to Characterize Respiratory Behaviors

by

Ang Chen

A Dissertation Presented in Partial Fulfillment
of the Requirements for the Degree
Doctor of Philosophy

Approved September 2020 by the
Graduate Supervisory Committee:

Yu (Kevin) Cao, Chair
Bertan Bakkaloglu
David Allee
Michael Goryll
Junseok Chae

ARIZONA STATE UNIVERSITY

December 2020

ABSTRACT

Respiratory behavior provides effective information to characterize lung functionality, including respiratory rate, respiratory profile, and respiratory volume. Current methods have limited capabilities of continuous characterization of respiratory behavior and are primarily targeting the measurement of respiratory rate, which has relatively less value in clinical application. In this dissertation, a wireless wearable sensor on a paper substrate is developed to continuously characterize respiratory behavior and deliver clinically relevant parameters, contributing to asthma control. Based on the anatomical analysis and experimental results, the optimum site for the wireless wearable sensor is on the midway of the xiphoid process and the costal margin, corresponding to the abdomen-apposed rib cage. At the wearing site, the linear strain change during respiration is measured and converted to lung volume by the wireless wearable sensor utilizing a distance-elapsed ultrasound. An on-board low-power Bluetooth module transmits the temporal lung volume change to a smartphone, where a custom-programmed app computes to show the clinically relevant parameters, such as forced vital capacity (FVC) and forced expiratory volume delivered in the first second (FEV_1) and the FEV_1/FVC ratio. Enhanced by a simple, yet effective machine-learning algorithm, a system consisting of two wireless wearable sensors accurately extracts respiratory features and classifies the respiratory behavior within four postures among different subjects, demonstrating that the respiratory behaviors are individual- and posture-dependent contributing to monitoring the posture-related respiratory diseases. The continuous and accurate monitoring of respiratory behaviors can track the respiratory

disorders and diseases' progression for timely and objective approaches for control and management.

DEDICATION

Dedicated to my whole family, whose love and support make all the impossible happened. My wife, Xu Han; my daughter, Anna Chen; my father, Jian Chen; my mother, Yanling Deng.

ACKNOWLEDGMENTS

I am lucky to have two such knowledgeable and supportive advisors in my Ph. D. study: Prof. Junseok Chae and Prof. Yu (Kevin) Cao.

I am so grateful to Prof. Junseok Chae for his mentorship. His contagious passion and perseverance on an exploration into research continuously drive me to move forward. Under his supervision, I have lots of freedom to explore and develop my topic. He is always there whenever I turn to him for help. It is very fortunate to have him be my advisor.

I would like to express my deepest gratitude to my second advisor Prof. Yu (Kevin) Cao. I have a minimum contribution to the NIMO group but gained unconditional support and meticulous care and attention from him. It is my treasure to have him be my advisor.

I am so honored to have Prof. David Allee, Prof. Bertan Bakkaloglu, and Prof. Michael Goryll serve as my committee members. Their comments and suggestions are valuable for me to enhance my knowledge and optimize my topic.

I want to show my thanks to all my co-authors, especially Prof. Ning Wu, who helps with custom-made app programming a lot and all the lovely colleagues in Prof. Chae's group: Dr. Hao Ren, Dr. Jennie Appel, Shiyi Liu, Jianwei Zhang, Seunghyun Lee, and in Prof. Yu (Kevin) Cao's group (NIMO group): Xiaocong Du, Zheng Li, and Zhenyu Wang.

TABLE OF CONTENTS

Page

APPENDIX Page

LIST OF FIGURES

CHAPTER 1

INTRODUCTION

1.1. Respiratory Mechanics

As a physiological activity, respiration is a systematic result of the nonlinear motion of the chest wall and the diaphragm. When the diaphragm contracts, the intercostal muscles in chest wall pull the ribs upward causing the rib cage to be enlarged in the pump handle movement. In elevation, the thorax's anteroposterior diameter increases and causes the lowermost ribs to swing outward, which is called the bucket handle movement, as shown in Fig. 1.1.

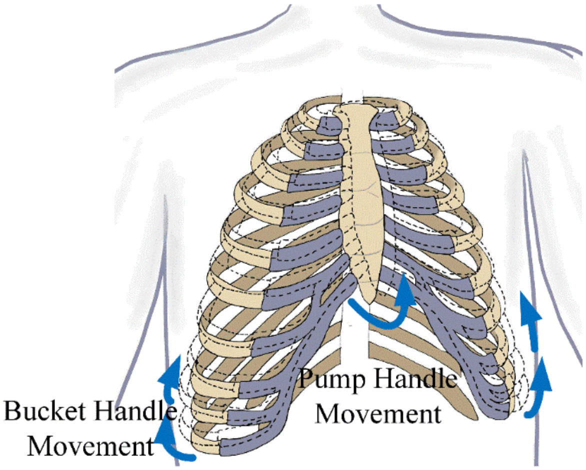

Figure 1.1. Pump Handle and Bucket Handle Movements.

Therefore, the horizontal enlargement of the thoracic cavity from the lifting of the front and sides of the ribs causes the circumference of the chest wall to increase during inspiration. With further movement of the diaphragm, the content in the abdomen was pulled outward, increasing the circumference of the abdominal wall; whereas in expiration, the intercostal muscles and diaphragm relax and passively restore to their anatomic positions determined by their anatomical elasticity, which pushes air out of the lung resulting in the circumferences of the chest and abdominal walls to decreases.

1.2. Methods for Respiratory Monitoring

Featured by its mechanics, respiratory monitoring can be realized by attaching various sensors on different location on human body.

Expiratory air is warmer, has higher humidity, and contains more CO_2 than inspiratory air, therefore in the oral/nasal area, relative humidity change [1, 2], temperature variance [3], and carbon dioxide production [4] within inspiration and expiration are primary parameters that are measured to monitor respiratory behavior. The respiratory sound caused by airflow through the trachea can similarly provide measurement: on the neck or throat, acoustic sensors, mainly made of piezo-material, are capable of collecting respiratory sound to extract respiratory rate [5, 6]. On the chest, respiratory monitoring has more options. Thorax pressure-induced variations in air volume within the lungs during inspiration and expiration provoke the transthoracic impedance change. The impedance change measured by skin electrodes correlates to respiratory rate [7]. Volume variations within the lungs provide a popular way for respiratory monitoring, measuring the circumferences of chest and abdomen change, such as inductance plethysmography, fiber-optic plethysmography, and strain-gauge, and so on. On the wrist, a watch/sport-band form pulse oximeter based on photoplethysmography(PPG) technique is used to measure the respiratory behavior through monitoring of O_2 and CO_2 concentration in arterial blood [8, 9].

All the wearable sensors are designed and developed to test the lung functionality, which, in turn, has a significant influence on respiratory behaviors.

1.3 A Protective Method for Acoustic Sensor Used in Respiratory Monitoring

Wearable sensors, especially acoustic sensors with membranes integrated to be the critical sensing elements, can be subject to external mechanical shocks, like dropping off against the ground, during deployment and operation. If severe enough, the shock load can cause irreversible damage to the acoustic sensors affecting its reliability and functionality. To mitigate the shock load, *Chen et al.* report a dual-membrane micro-electromechanical system(MEMS) that can effectively reduce the sensing membrane's travel distance upon deploying low voltages [10]. It is a simple yet effective structure with an addition of a second membrane on top of the traditional single membrane structure(Fig. 1.2(a) and (b)). The bottom sensing membrane can perform stable oscillation within the safety zone by utilizing the applied electro-statistic force and membrane inherent restoration force. The dual-membrane structure photos are shown in Fig. 1.2(c) and (d).

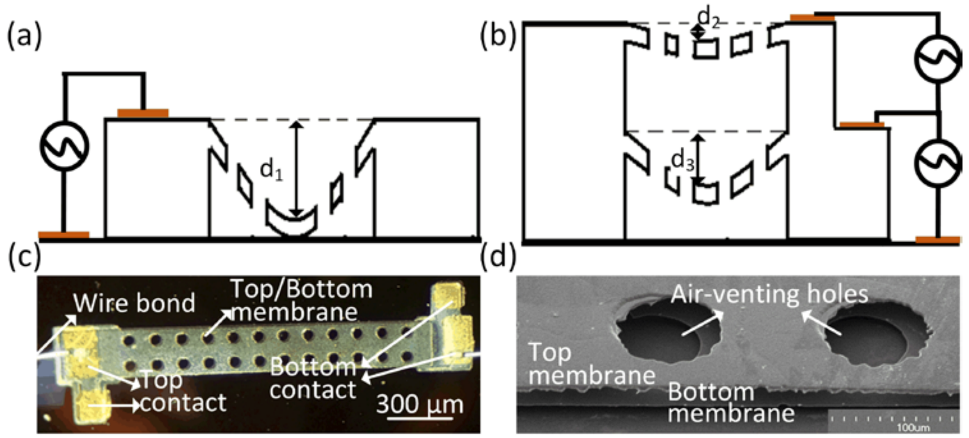

Figure 1.2. Schematic and Photos of the Dual-membrane Structure. (a) A conventional single movable membrane upon shock. (b) Dual-membrane structure with an additional top membrane and a movable bottom membrane upon shock. (c) Top view of the fabricated dual-membrane device. (d) Cross-section view of the fabricated dual-membrane device.

To implement *in-situ* control of electrostatic force, a microcontroller and an accelerometer were used to control the timing of electrostatic force upon a shock. When the accelerometer's output exceeded a threshold, the microcontroller sent a command to apply an electrostatic force within the peak shock amplitude period of around 500 μs. The force was applied between the top and bottom membranes to mitigate the shock effect before the bottom membrane reaches its maximum travel distance. Thus, the timing scheme prevented the bottom membrane from hitting the substrate. To evaluate the effectiveness of *in-situ* control, we dropped the board containing an accelerometer trigger and a microcontroller. The *in-situ* control is capably implemented electrostatic mitigation, as shown in Fig. 1.3.

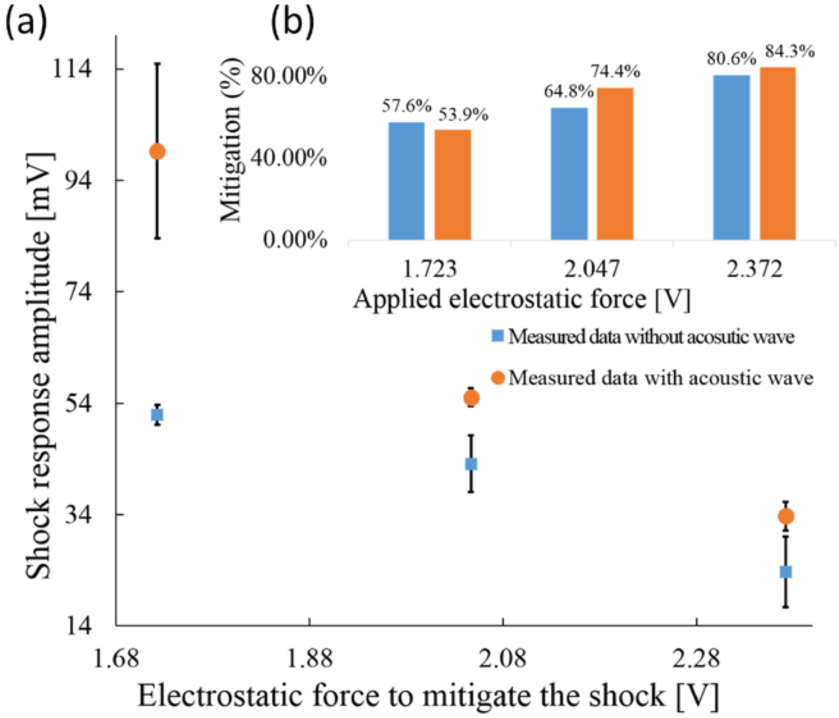

Figure 1.3. In-situ control of shock-mitigation: (a) Shock response with different electrostatic force, 1.723 V, 2.047 V, 2.372 V separately. (b) Shock mitigation percentage versus applied electrostatic force between top and bottom membranes.

For more details about the MEMS structure to mitigate the external shock, please see appendix B.

1.4. Burden of Respiratory Diseases

Respiratory diseases, a significant worldwide health challenge, are responsible for more than 10% of all disability-adjusted life year (DALYs): a metric used in public health and health impact assessment that estimates the number of years of healthy life lost due to ill-health, disability or early death. Mortality, disability, and morbidity caused by respiratory diseases, which are second only to cardiovascular diseases, imposed immense economic costs and health burden worldwide. Among respiratory diseases, chronic obstructive pulmonary disease (COPD) and asthma predominantly contribute to the burden. An estimated 65 million people have moderate to severe COPD, of which about 3 million die each year, making it the third leading cause of death worldwide, and the frequency of the disease remains increasing trajectory. About 334 million people have asthma, which is the most common chronic disease of childhood, affecting 14% of children globally. The prevalence of asthma in children keeps rising. Alternatively, sleep-disordered breathing is a less well-quantified respiratory disorder, and more than 100 million people are suffering from it.

1.4.1 Need of Continuous Monitoring

Characteristics of respiratory diseases suggest continuous monitoring of respiratory behaviors benefit patients. COPD and asthma, the two most common respiratory diseases, are characterized by airway inflammation, which causes breathlessness in terms of an extrinsic failure of the chest wall to obtain and maintain sufficient lung volume. However, symptoms of the changeability on COPD and asthma have been studied and described as time-dependent, even over one day, thus it is challenging to generalize the characteristics of respiratory behaviors. The diagnosis of respiratory diseases is based on the history of patients, symptoms, and the outcome of attempted therapies. Therefore, the continuous monitoring of the respiratory behaviors offers valuable information to the pre-diagnosis by extracting the clinically relevant parameters to describe the progression of patients' respiratory conditions.

1.4.2 Need of Wireless Wearable Sensor

The current clinically approved method to characterize lung function is spirometry using a spirometer. A spirometer is a physiological test that measures how an individual inhales or exhales volumes of air as a function of time. The primary signal measured in spirometry may be volume or flow. Characterized by its prohibitive cost and large size, the affordability of continuous respiration monitoring is mostly limited. Additionally, some respiratory diseases are periodic; the spirometry tests may yield normal results even when the individual does contain abnormal lung conditions, such as asthma. Besides, asthma attacks often happen in the early morning or late at night, making the supervision more difficult than in the daytime. If insufficient careful supervision is not given, especially for children, unexpected consequences can happen.

1.5. Summary of Chapters

To provide continuous respiratory monitoring, characterize the respiratory behavior, and contribute to respiratory disease management and control, a wireless wearable sensor/system is proposed. The second chapter includes a wireless wearable sensor to characterize respiratory behaviors, extracting the $FEV_{1/}FVC$ ratio for caregivers to provide proper medical intervention to people who have asthma. In chapter 3, a system consisting of two wireless wearable sensors is able to predict human postures based on extracted respiratory features from general respiration among the various subjects. The system can be used to study respiratory individuality contributing to posture-related respiratory diseases.

CHAPTER 2

WIRELESS WEARABLE ULTRASOUND SENSOR ON A PAPER SUBSTRATE TO CHARACTERIZE RESPIRATORY BEHAVIOR

2.1. Introduction

Asthma is a significant worldwide health problem affecting between 1-18% of the population in different countries [11]. Over the last 40 years, the global burden due to prevalence, morbidity, mortality, and economics associated with asthma has increased significantly. With an increase of 50% every decade, approximately 300 million people worldwide currently have asthma [12]. In the United States, about 25 million people are plagued by asthma, corresponding to approximately one out of every 12 people. Asthma is a severe disease affecting all age groups, particularly children. Approximately 7 million children in the United States are diagnosed with asthma [13]. With asthma, the hypersensitivity of the airways causes inflammation due to the exposure to asthma triggers, such as common cold, stress, changes in the weather, or things in the environment daily. This hypersensitive state could make the airway swell even more, narrowing the space for air to move in and out of the lungs resulting in a severe obstruction and even death. If more than one typical asthma symptom is present, then the probability of having asthma increases, especially in adults. These symptoms, when described in medical terms, include forced expiratory volume delivered in the first second (FEV1) of a forced vital capacity (FVC) maneuver and the ratio of FEV1 to FVC [14-20]. A reduced FEV_1 may be found with many other lung diseases; however, a reduced FEV1/FVC ratio indicates airway inflammation. According to population studies, the

FEV_1/FVC ratio usually ranges > 0.75 to 0.8 for adults and > 0.9 in children. Any values less than these suggest airflow limitation [11, 21].

The characteristics of asthma stress the importance and need for continuous respiratory behavioral monitoring. It is characterized by chronic airway inflammation and is defined by the history of respiratory symptoms such as wheezing, shortness of breath, chest tightness, and coughing that vary over time and intensity, together with variable expiratory airflow limitation [11]. The diagnosis of asthma is made clinically based on the patient's history, symptoms, and response to therapy [22]. Diagnosis based on symptoms alone is not clinically approved since other health conditions can mimic asthma symptoms. For example, vocal cord dysfunction can cause difficulties in breathing, and immunodeficiency, ciliary dyskinesia, cardiomyopathy, or cystic fibrosis may all present with respiratory symptoms, including airway obstruction. The challenge of symptom-driven diagnosis escalates for infants and young children, whose small airways become obstructed more easily and whose response to the treatment often is equivocal [23]. Thus, the documented daily respiratory behavior parameter, specifically the FEV_1/FVC ratio, helps with asthma diagnosis and control [11]. Asthma patients show FVC marks nearly normal [24, 25], and an out of range FEV_1/FVC ratio indicates airway inflammation reminding people to seek medical intervention. Proper medical intervention and a good adherence to the prescribed medicine can effectively control asthma [26-33].

The current clinically approved method to characterize lung function is spirometry. Spirometry is a physiological test that measures how an individual inhales or exhales volumes of air as a function of time. The primary signal measured in spirometry may be volume or flow. Characterized by its prohibitive cost and large size, the affordability of continuous respiration monitoring is mostly limited. Additionally, some forms of respiratory diseases are periodic; the spirometry tests may yield normal results even when the individual does contain abnormal lung conditions, such as is the case with asthma [34].

Many groups have explored sensors for respiratory behavior monitoring. Some of these sensors consist of embedded coils around the abdomen and the chest, detecting the chest wall circumference change to monitor respiration by inductance plethysmography [7, 35]. Davis et al. reported a fiber-optic strain gauge around the abdomen and chest to do respiratory monitoring using fiber-optical plethysmography [36]. Others utilized a resistive strain gauge sensor around the abdomen and chest to measure the chest wall circumference change to monitor respiration [37]. Wehrle et al. reported a strain sensor taking advantage of the Bragg grating effect to monitor respiratory movements with frequency components up to 10 Hz [38]. An expandable belt sensor was used with embedded optic fibers wrapped around the chest to monitor similar high-frequency oscillatory ventilation, which measures the loss of light transmitted in the fiber due to the alterable curvature induced by circumference change to monitor respiration [39]. A monitoring system based on measuring respiration signals by detecting the attenuated reflected ultrasound signal can also monitor the anterior-posterior motion of the chest wall [40]. Many other groups reported alternative respiratory monitoring sensors [41-45]. Friat et al. designed a paper sensor exploiting the hygroscopic feature of cellulose paper with digitally printed graphite electrodes. The sensor measures the respiration rate by detecting the moisture adsorbed on the paper, from inhaled and exhaled air, attached inside a flexible textile procedure mask [46]. Yan et al. reported a respiration sensor having stretchable nitrile rubber films. The stretchable films allow the enhanced capability of detecting the various intensities of respiration. The electrodes on the films measure the current to correlate the breathing rate [25]. However, almost all prior sensors record the respiratory rate, which has a relatively limited clinical value [47], and few contribute to asthma control by providing useful vital respiratory information with significant clinical value, such as the FEV_1/FVC ratio.

To contribute to asthma control, this work presents a wireless wearable sensor that offers continuous measurement of respiratory behavior coupled with a mobile app to extract clinically-relevant parameters to describe the progression of the respiratory diseases such as asthma, resulting in properly seeking medical care before an asthma attack occurs.

2.2 Material and Method

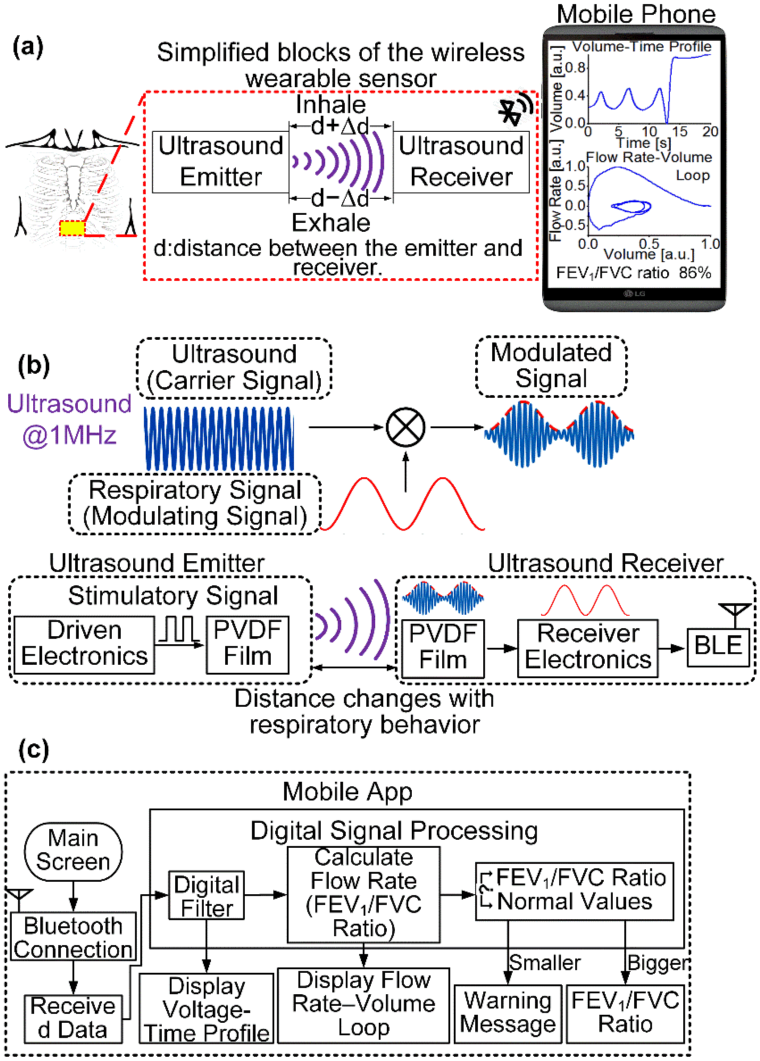

Figure 2.1. Schematic Diagram of Wearable Sensor System. (a) The wearable wireless sensor, attached on the midline of the chest, measures a local strain of chest circumference as a function of time, to characterize respiratory behavior. The local strain is measured by a modulated signal on an ultrasound carrier. The temporal data is processed onboard and transmitted to a smartphone where a custom-made app displays respiratory behavior plots and computes clinically relevant quantitative parameters. (b) Operating principle of the sensor. The ultrasound carrier, generated by on-chip ultrasound emitter, is mixed with the respiratory signal, from the local strain of the chest circumference. The mixed modulated signal is processed onboard and transmitted to a smartphone via Bluetooth. (c) The custom-made mobile app receives the data and uses DSP (Digital Signal Processing) filters and calculates clinically-relevant respiratory behavior parameters: FEV$_1$ (Forced Expiratory Volume delivered in the 1st second) and

FVC (Forced Vital Capacity), and the FEV_1/FVC ratio. Then, the app displays temporal tracing and differential plots that show the respiratory behavior in pseudo-real time.

2.21 Wireless Wearable Sensor

The wireless wearable sensor is designed to characterize respiration by analyzing the circumference changes in a person’s chest during respiration. The localized change of the chest wall's circumference effectively emulates the lung volume behavior during the respiration. When the diaphragm contracts, the intercostal muscles pull the ribs upwards, causing the rib cage to be enlarged in the pump handle movement. In elevation, the thorax's anteroposterior diameter increases and causes the lowermost ribs to swing outwards, which is called the bucket handle movement. Therefore, the horizontal enlargement of the thoracic cavity from the lifting of the front and sides of the ribs causes the chest wall's circumference to increase during inspiration. During expiration, the diaphragm and intercostal muscles relax. The chest and abdomen passively return to a position determined by their anatomical elasticity, which results in a decrease in chest circumference [48, 49]. The sensor is designed to measure the localized strain of chest wall circumference, comprising an ultrasound emitter used to emit ultrasound and an ultrasound receiver to receive the distance-elapsed attenuated ultrasound, as shown in Fig. 2.1(a). During inspiration, the ultrasound emitter and receiver move further apart, resulting in a more attenuated ultrasound signal, whereas the emitter and receiver move closer together in expiration, resulting in an increased ultrasound signal. To generate the ultrasound, a non-polarized pulse stimulatory signal is applied to a piezoelectric material, Polyvinylidene Difluoride (PVDF) film [50-53]. The PVDF film generates mechanical deformation upon an electric field being applied across the film, and the mechanical strain follows the electrical field's frequency. In this work, we used a 1 MHz electrical field to generate a 1 MHz ultrasound. The ultrasound is modulated by the respiratory signal and received by another PVDF receiver. After demodulation and amplification, the respiratory signal is extracted, and the digitized respiratory signal is then wirelessly transmitted to a mobile phone by the onboard Bluetooth antenna, a process shown in Fig. 2.1(b).

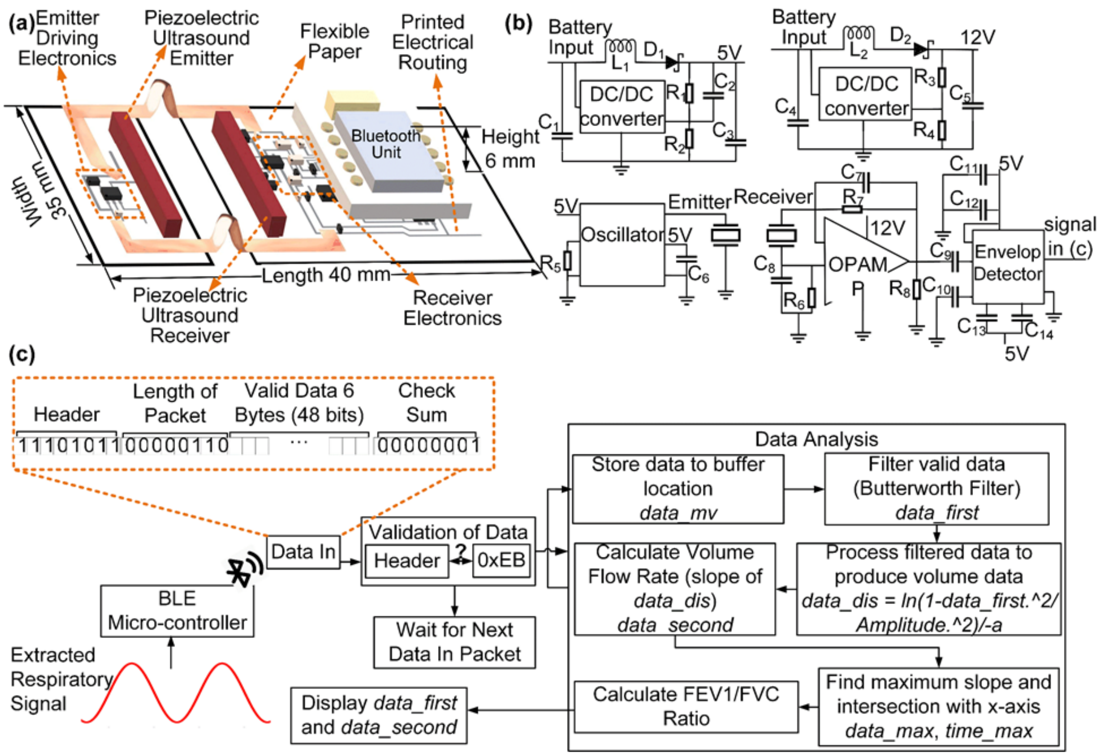

Figure 2.2. Circuit Diagram and Custom-made Mobile App Algorithm Blocks. (a) Fully-assembled wireless wearable sensor: the low-profile sensor has a footprint of 40 mm × 35 mm × 6 mm on a paper substrate, including emitter driving electronics to excite a piezoelectric PVDF film to emit ultrasound wave, receiver electronics to convert the modulated ultrasound wave to an electrical signal, and a Bluetooth module to digitize the electrical signal and send it to mobile app wirelessly. (b) The sensor's circuit diagram: wireless sensor electronics consist of two DC-to-DC converters to provide adequate power to corresponding electronic modules, an op-amp to amplify the modulated signal, and an envelope detector to extract respiratory behavior signal for wireless transmission. (c) The extracted respiratory behavior signal is digitized and coded by onboard micro-controller into four kinds of strings: header, length of the packet, valid data, and

checksum. Then the strings are sent to a custom-designed mobile app wirelessly by Bluetooth. The app analyzes the transmitted data, including checking the header for validity, filtering the valid data, and extracting the clinically relevant parameters.

2.2.2 Fabrication of the Wireless Wearable Sensor

The wireless wearable sensor's overall schematic is illustrated in Fig. 2.2(a), and the photos of the sensor are in appendix C. The sensor's footprint and weight are 40×35×6 mm^3 and 6.5 g, including 2.7 g battery, respectively. The conductive electrical traces for the sensor was printed, by a laser printer, on a paper substrate (OL177WS, Online Labels, Inc.). A pea-sized amount of silver epoxy (Atom A-DUCT-1, Atom Adhesive Inc.) was squeezed out on the printed circuit and was spread evenly over the entire circuit manually. Hot air (~200 °C) was blown over the entire circuit in a lateral motion for 1 minute to dry out the silver epoxy and melt the toner particles. The toner contains carbon and iron oxide, polypropylene, fumed silica, and various minerals for triboelectrification. It is primarily composed of granulated plastic that can form a bond between the silver epoxy and the glossy paper in the circuit's shape as it melts.

The paper substrate is made with a layer of white clay called kaolin that fills between the paper fibers to produce a smooth surface. The organic mixture of silver epoxy is incapable of adhering to the kaolin surface, allowing easy removal of excess epoxy using a cotton ball. These two steps were repeated until the silver epoxy on the circuit lines became fully conductive. The finished lines have a conductivity of 0.9 Ω/cm with a width of 0.3 mm. A different silver epoxy, having higher adhesion than the one above (Electron Microscopy Sciences, 12642-14 two-part conductive silver epoxy), was used to mount the electrical components on the printed circuit. A 110-µm thick PVDF film (3-1003702-7, TE connectivity Inc.) having electrodes sputtered by 70nm/10nm of copper and nickel on both sides was attached to a rigid paper sheet using double-sided tape for standing support, and the copper tape was used to connect the PVDF films to the circuit due to its characteristic robust connection [54]. The copper tape serves as the electrical bridges between the two pieces of the emitter and receiver pieces as well.

2.2.3 Electronics of the Wireless Wearable Sensor

The schematic of electronics being used for the wireless wearable sensor is shown in Fig. 2.2(b). A micropower DC/DC converter (LM2704, Texas Instruments Inc.) steps up 3.7 V of lithium battery to 5 V or 12 V with current limits of 120 mA or 40 mA, respectively. A voltage-controlled oscillator (LTC6990, Analog Devices Inc.) excites the emitter's PVDF film to generate a 1 MHz ultrasound. Another PVDF film detects the ultrasound signal modulated by the respiratory signal. Connected afterward is a low noise, FET-input operational amplifier (OPA657 from Texas Instruments Inc.). Characterized by a high gain-bandwidth product (1.6 GHz) and low voltage noise JFET-input stage, a very low-level signal can be significantly amplified by a single OPA657 stage, offering 1600 V/V(64 dB) for a 1 MHz signal. Following amplification, an envelope detector (ADL 5511, ADI) extracts the respiratory signal, which is then sent to a Bluetooth Low Energy Nano V2 (RedBearLab) using 100 Hz sampling frequency with ultra-low power consumption. The BLE (Bluetooth Low Energy) device uses an onboard analog to digital converter (ADC) with a 12-bit resolution to digitize the analog input signal before transmitting it to external Bluetooth devices for analysis.

2.2.4 Mobile App

The simplified diagram of the custom-designed app's algorithm is shown in Fig. 2.2(c), and more details are in appendix E. The mobile application receives the signal and filters it by Butterworth low-pass filter with the cut-off of 0.5 Hz to display primarily two graphs: the temporal trace of the voltage corresponding to volume vs. time and the flow rate vs. volume plot. The second graph is used to determine the FEV_1/FVC ratio, which is then compared to the nominal value of 0.75. The American Thoracic Society has identified the back-extrapolation method as the most consistent and accepted technique for determining the start point and has recommended its use for every calculation of FEV_1. The extrapolated volume should not be higher than 5% of the FVC or 150 mL; whichever number is higher [55]. Instead of getting extrapolated volume in Spirometry, the extrapolated voltage was defined for the wireless wearable sensor. It is for the correlation between the wireless wearable sensor's output with a unit of voltage and the output of the spirometer test with a unit of milli-liter or liter. To determine the extrapolated voltage, a differential analysis of the temporal output was used to find the deep expiration curve section with the greatest tangential slope. The most significant value, the previous data point, and the following data point were used to plot a trend line. From the equation of the trend line, the intersection with the x-axis can be found. This x-intercept is the new start time (t=0), and the corresponding y-axis value y_0 on the voltage-time graph is the extrapolated voltage. The point on the x-axis, which is one second afterward, is designated t=1, with the corresponding y-axis value designated as y_1. Regarding the maximum voltage as the FVC and FEV_1 as y_1-y_0 with a unit of voltage, then

$$FEV_1/FVC\ ratio = \frac{y_1 - y_0}{maximum\ voltage} * 100\%$$

Once the FEV_1/FVC ratio reaches below 75%, a warning message will show on the mobile phone screen to inform the abnormal respiratory behavior (Fig. 2.1(c)).

2.2.5 Study Design

We studied the wireless wearable sensor's efficacy and accuracy to monitor respiratory behavior based on anatomical and experimental analysis. To demonstrate the feasibility, we recruited volunteers to attach the wireless wearable sensor on their bodies to collect respiratory parameters. Randomization was not applicable, and investigators were not blinded. All participants provided informed consent, and the studies were approved by the Arizona State University Institutional Review Board (IRB).

2.2.6 Respiratory Behavior Collecting Protocol

Miller et al. published the standardization of spirometry in 2005, putting official statements of the European Respiratory Society (ETS) and American Thoracic Society (ATS) together [56]. Following the standardization of spirometry, first, we demonstrate the study procedures to volunteers. We attached the wearable wireless sensor to the volunteers to simultaneously collect the respiratory parameters from the spirometer and the sensor. The volunteers hold a breathing tube that is sealed around a mouthpiece. The volunteers perform three cycles of routine respiration sequence of inhaling and exhaling. For forced vital capacity (FVC), the volunteers inhale fully and rapidly and exhale with maximum effort.

2.2.7 Benchmark Comparison of Wireless Wearable Sensor to Spirometer

Eight volunteers were included in this study. In a sitting position with a nose-clip, each volunteer completed three regular breathing cycles through the mouthpiece. On the fourth cycle, the volunteer took a deep breath in and exhaled thoroughly as brief a time as possible to maximize the airflow in the first second and keep exhaling at least 6 seconds to ensure a complete test result. During the procedure, volunteers were asked to keep their backs straight. Keeping backs straight allows the rib cage not to weigh on the abdomen and the abdominal wall to maximize the accuracy [57]. After proper relaxation, the wireless wearable sensors were placed at the designated location, and the volunteers repeated the procedure. Due to its compact size and wearability, the wireless wearable sensor has a limited effect on the spirometry test, and so both sensors were used simultaneously to eliminate as many variables as possible.

2.3 Results and Discussion

2.3.1 Positioning the Wireless Wearable Sensor

The wireless wearable sensor was placed on four locations of the chest wall, including the right side of the chest wall, the upper chest wall, the upper back of the chest wall, and the midway between the xiphoid process and the costal margin, as shown in Fig. 2.3(c). The best conversion of chest wall circumference change was obtained from the sensor located between the xiphoid process and the costal margin, corresponding to the abdomen-apposed rib cage. The theoretical and experimental analyses finalized the location for the sensor. To verify the designed properties of wear-ability and effectiveness in long-term daily monitoring, we attempted to test the sensor in the two dynamic situations of walking and running, approximately 1.2 m/s and 2 m/s for 20 secs, respectively, with results shown in Fig. 2.3(d). The respiratory rates were five and seven times in 20 seconds, for walking and running, respectively. The most prominent artifact from human body movement includes vertical up and down motion when the subject walks or run. Fig. 2.3(d) shows that the body's slight movement has little impact on the quality and the distinguishability of data. The motion artifact may impact large and heavy wearable sensors due to the moment of inertia, but the lightweight 6.5 g sensor showed little motional artifact. The emitter and the receiver are symmetrically located on either side of the midway of a human chest; thus, the common-mode movement cancels out each other. Assuming little misalignment exists between PVDF films of the emitter and the receiver, the collected signal maintains stable throughout the body movement, highlighting the wearability of the wireless wearable sensor.

2.3.2 The Characterization of Wireless Wearable Sensor

The wireless wearable sensor's functionality should maintain at a given curvature on the body where the sensor is located. As the distance changes between the emitter and receiver, the corresponding ultrasound pressure changes at curvatures of 0 m-1, 1.44 m^{-1}, 1.74 m^{-1} and 2.13 m^{-1}, as shown in Fig. 2.3(a). The curvatures experiments cover the range of the chest wall curvatures effectively [58]. Fig. 2.3(b) shows the sensor's output voltage as a function of normalized pressure at the receiver, demonstrating excellent linearity. The theoretical supporting material is in appendix D.

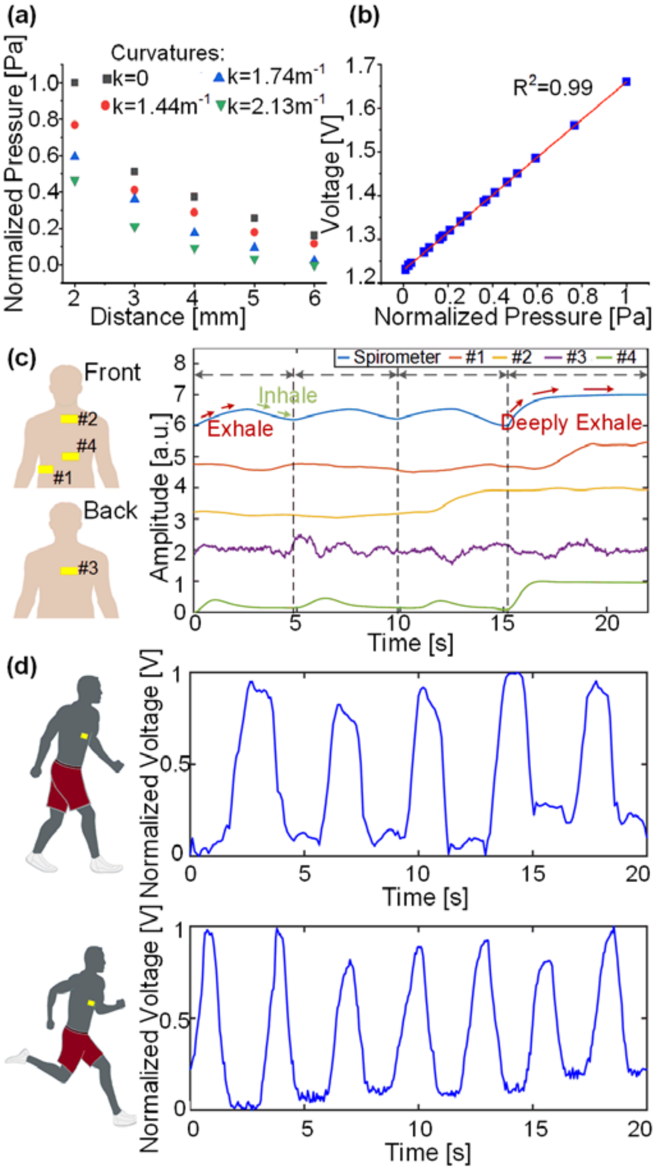

Figure 2.3. Ultrasound Principle, Optimum Placement, and Dynamic Test Verification. (a) Normalized ultrasound pressure is a function of the distance between the ultrasound emitter and receiver, on the surfaces of different curvatures: the pressure decreases as the distance increases because the attenuation of ultrasound wave increases. The trend shows a consistent pattern on different curvature of flat (k=0) and largely curved (k of up to 2.13 m^{-1}) (b) The output voltage of the wireless wearable sensor as a function of normalized pressure applied to the PVDF film: the output of sensor shows a very linear response to the normalized pressure that is a function of the distance between ultrasound emitter and receiver. (c) Experimental results of the sensor on four chest locations: this is to find the most appropriate location for the sensor to effectively characterize the respiratory behavior. #4 is chosen because the location agrees well with

anatomical analysis, and the measured pattern of the sensor shows very similar to that of a spirometer. (d) Dynamic characterization of the sensor when a volunteer is walking and running with a speed of 1.2 m/s and 2 m/s for 20 seconds, respectively.

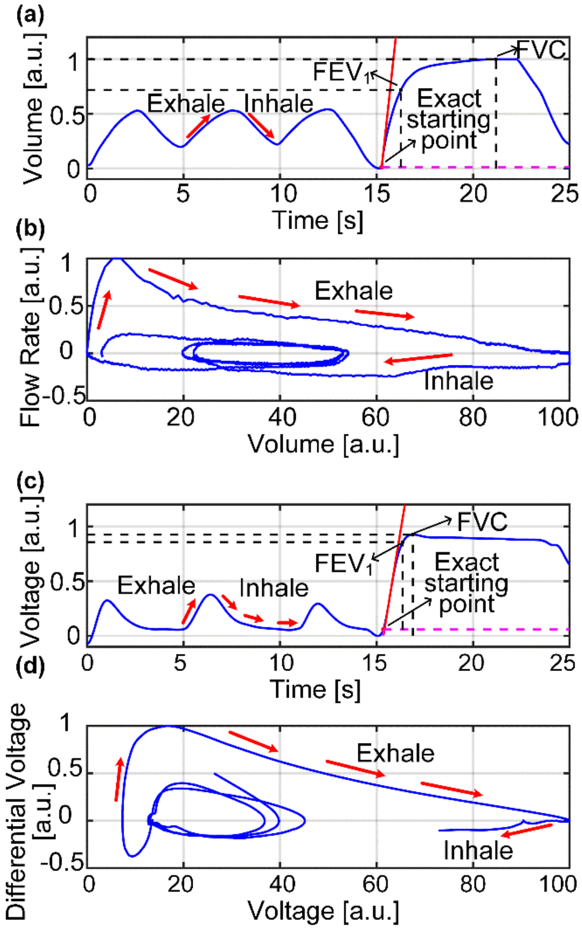

Figure 2.4: Respiratory Volume- and Flow Rate-Volume Results Comparison Between Wearable Sensor and Spirometer. (a & b) Spirometer and wireless wearable sensor (c & d): (a) and (c) are volume-time tracing with marked FEV_1, FVC, and extrapolated volume, whereas (b) and (d) are flow rate vs. volume for spirometer and wireless wearable sensor, respectively. Clinically relevant parameters, including FEV_1 and FVC, are computed from spirometer and sensor, respectively, to be compared side by side.

2.3.3 Temporal Output profile of spirometer vs. the wireless wearable sensor

The respiratory behavior plots of the spirometer (Pneumotrac Spirometer, Model 6800, Vitalograph Inc.) and wireless wearable sensor, following the standard protocol, are shown in Fig. 2.4. The temporal output profile of the sensor, Fig. 2.4(c), has a strong correlation with that of the spirometer, Fig. 2.4(a). Both start with a general expiration pattern, shown by the tracings both trending upwards and exhibiting the similar respiration behaviors. The sensor illustrates inhalation behavior slightly earlier than the spirometer does. This may be due to the inherent discrepancy between direct and indirect measurements of lung volume. The spirometer directly measures the flow out of the lungs through the mouthpiece, whereas the sensor indirectly measures the lung volume via the circumference change of the chest wall. Several reported the chest wall's circumference change occurs before the start of inspiration and expiration due to the mechanics of respiration [48, 59]. For the fourth deep expiration, since the volunteer was purposely exhaling as fast as possible, the minimal time delay was observed in both temporal plots. The sensor's temporal output was used to obtain the volume flow rate graph shown in Fig. 2.4(d), which is comparable to the flow-volume tracing of the spirometer in Fig. 2.4(b). Both start with the general respiration (small loops in the figures), and once volunteers perform the forced expiration, the curve rapidly mounts to a peak, known as the peak expiratory flow (PEF). After the PEF, the curve descends, representing the decreasing flow as more air is exhaled. A straight or a convex tracing from PEF to FVC point (the greatest intercept on the x-axis) would indicate non-pathological respiratory behavior. In results from both the spirometer in Fig. 2.4(b) and the sensor in Fig. 2.4(d), a convex tracing was observed, meaning the respiratory behavior for this specific attempt on the volunteer is normal [55, 56]. The FEV_1/FVC ratios of 86% and 87.94% were achieved by spirometer and the sensor, respectively, supporting the sensor is capable of measuring the normal respiratory behaviors. The measurement of sub-optimal respiratory behavior is in appendix F.

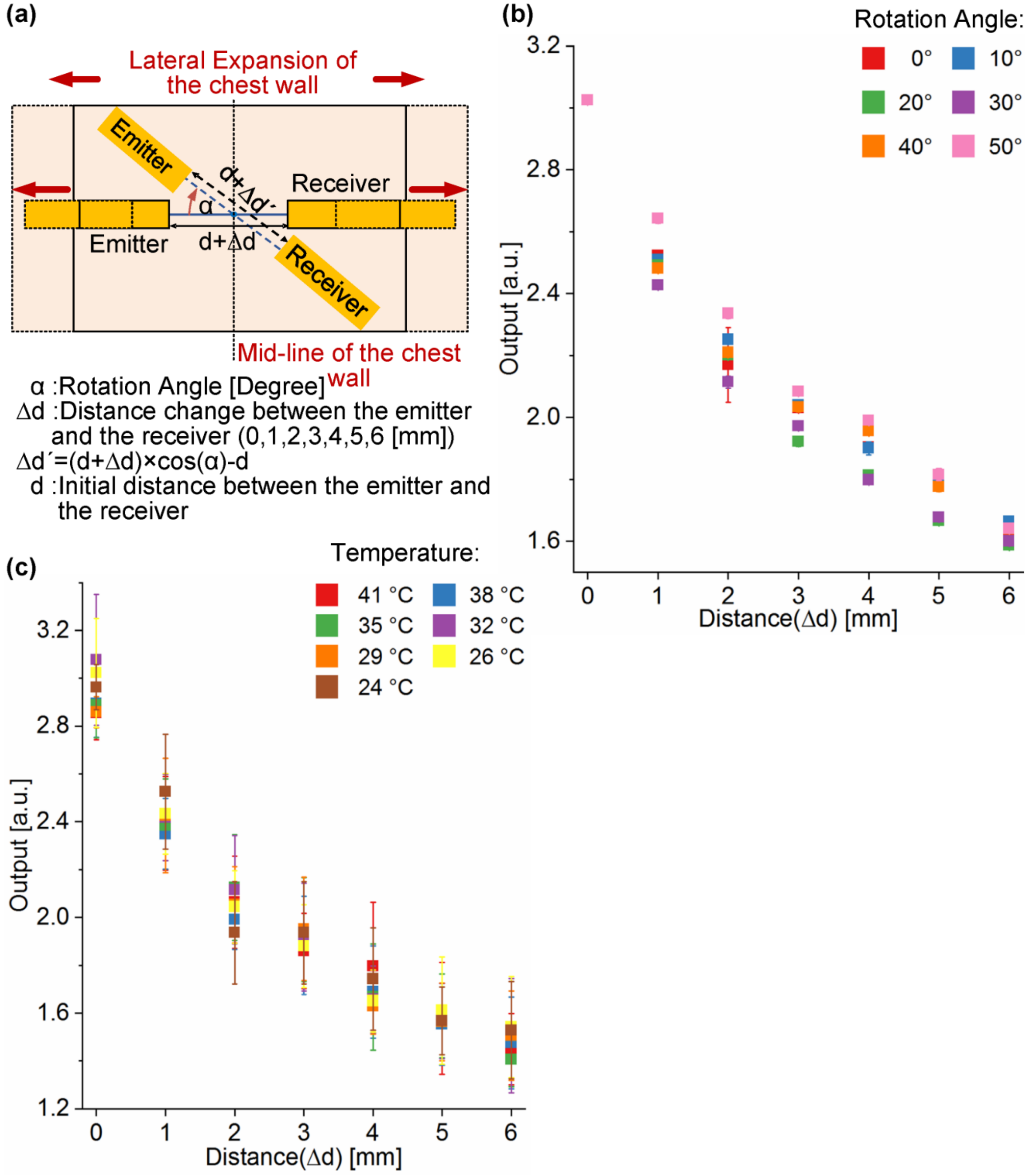

Figure 2.5: Placement Influence Analysis in Practical Settings (a) The wireless wearable sensor has been tested at different rotation angles with the increase of the distance between the emitter and the receiver from 0 mm to 6 mm at 1 mm distance interval in the horizontal direction to demonstrate continued functionality with sub-optimal sensor

placement. (b) At a given rotation angle, the output decreases as the distance between the emitter and the receiver increases. The sensitivity, the slope, decreases as the angle increases because the effective distance between the emitter and the receiver decreases. (c) Temperature sensitivity of the sensor: the sensor was tested under different temperatures, ranging from 24 °C to 41 °C, demonstrating rather insensitive to ambient temperature change.

The output signal can get the best illustration from the horizontally located wireless wearable sensor since the chest wall's lateral expansion is more significant. However, a user may not place the wireless wearable sensor exactly where it is designed to be, resulting in finite error at the sensor output. The wearable wireless sensor was tested at different angles with the increase of the distance between the emitter and the receiver ranging from 0 mm to 6 mm with a 1 mm interval in the horizontal direction to verify the sensor is capable of working properly in non-ideal positions. When the rotation angle is zero, the horizontal movement equals the distance change between the emitter and the receiver, as shown in Fig. 2.5(a). The effective distance between the emitter and the receiver is a function of the rotation angle. As the rotation angle increases, the effective distance decreases, thus the sensitivity, the slope of the output vs. distance, decreases, as shown in Fig. 2.5(b). All the starting points have been overlapped together for easy comparison of the rotation angles' effect on the wireless wearable sensor. The experimental results show the sensitivity suffers by 5%, 8%, 3%, 2%, and 1% from the human-error induced rotation of 10°, 20°, 30°, 40°, and 50°, respectively. The loss of sensitivity impacts the critically relevant parameter, FEV1/FVC, by 8%, supporting that the wireless wearable sensor offers acceptable performance within a reasonable angle of rotation.

The body itself provides a rather isothermal setting, yet the operating temperature of the wireless wearable sensor may change as a function of external temperature. The sensor was tested under temperatures ranging from 24 °C to 41 °C to study the temperature sensitivity. The sensor outputs were recorded at the distance of 0-6 mm from 24 °C to 41 °C, as shown in Fig. 2.5(c). While slightly varying outputs were observed, the outputs variation was within measurement errors, demonstrating that the temperature effect on our sensor is very limited.

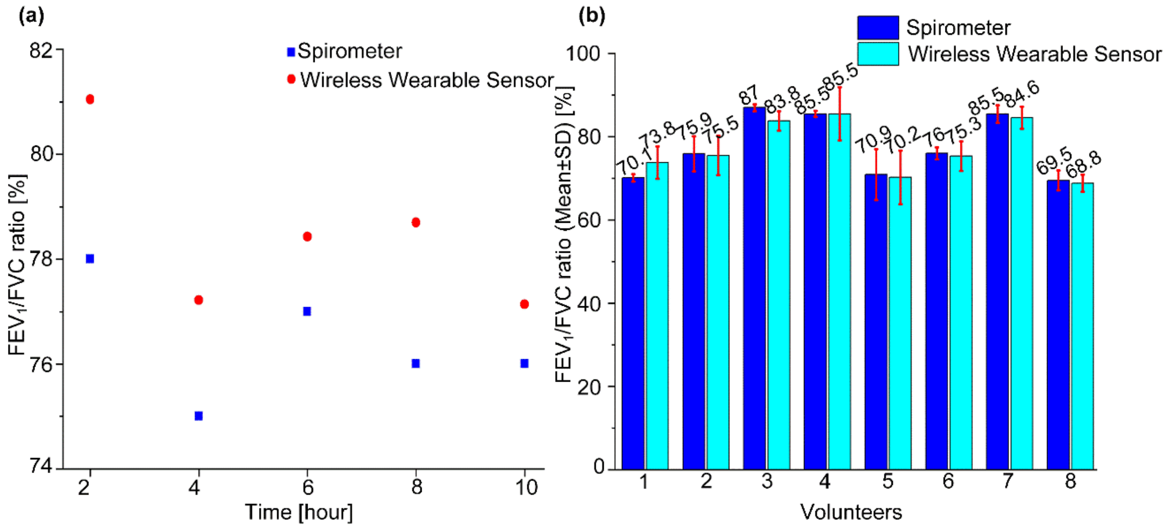

Figure 2.6: Longitudinal Experiments and Spirometry Test Summary (a) The FEV$_1$/FVC ratio of a volunteer wearing the wireless wearable sensor at 2-hour, 4-hour, 6-hour, 8-hours, and 10-hours. (b) The FEV$_1$/FVC ratio of the spirometer and the sensor: the mean differences between the spirometer and the sensor range from 0.00% to 4.25%, demonstrating the excellent correlation of the ratio between the spirometer and the sensor attempts.

Wearable sensors that monitor physiological parameters are preferred to demonstrate robust performance over time. The time-elapsed FEV$_1$/FVC ratio from the spirometer and the wireless wearable sensor over ten hours is shown in Fig. 2.6(a). The FEV$_1$/FVC uncertainties range from 1.86% to 3.91% over five trials, showing finite uncertainties over time. When the need of long-term daily monitoring of respiratory behaviors outlasts the accuracy requirement, the use of sensor may justify the moderate error as a spirometer possesses challenges on such task. Moreover, the sensor allows respiratory behavior monitoring at targeted time windows, such as at night or early morning, when asthma symptoms are more severe than at the clinic [60]. A summary of FEV_1/FVC ratios of the spirometer and the sensor of eight volunteers are shown in Fig. 2.6(b). The mean differences between the spirometer and the sensor range 0.00% - 4.25%. Despite the low number of volunteers, the mean differences show consistency and demonstrate the accurate measurement capabilities of the sensor. The maximum mean error marks merely 4.25%, which may be sufficiently accurate to monitor the FEV_1/FVC ratio effectively and warn care-givers to seek proper medical intervention before an asthma attack.

2.4 Conclusion

The wireless wearable sensor utilizes piezo material (PVDF film) to generate and receive an ultrasound to monitor respiratory behaviors by measuring the change of the circumference of the chest wall, which has a linear relation to the vital volume change. The amplitude of ultrasound is modulated by inhaling/exhaling behaviors due to the changing distance between the ultrasound emitter and the receiver. With the increase and decrease of the chest wall's circumference, causing more and less attenuation of the ultrasound pressure, the output of the wireless wearable sensor is similarly increasing and decreasing, which defines the inspiration and the expiration, respectively. This is used to characterize the respiratory profile to obtain the FEV_1/FVC ratio to help asthma control.

Dynamic characterization, including walking and running while wearing the sensor, verifies the wearability of the sensor. Furthermore, the comparison between a spirometer and the sensor highlights the sufficiently accurate results of a mean difference ranging from 0.00 % to 4.25 %.

Some challenges remain for the wireless wearable sensor. The sensor indirectly measures the volume change during respiration by measuring the circumference change of the chest wall; these featured movements of the human chest wall will inevitably induce some indirect measurement uncertainty. To precisely estimate the volume, we need sophisticated computation to find a proper relation to converting the circumference change to volume change. We believe the discrepancy can be compensated and minimized by advanced computation techniques in the future. In addition, the accuracy and utility of the sensor may be enhanced by adopting moisture absorbable layer or stretchable films [25, 46, 61].

CHAPTER 3

MACHINE-LEARNING ENABLED WIRELESS WEARABLE SENSORS TO STUDY INDIVIDUALITY OF RESPIRATORY BEHAVIORS

3.1 Introduction

Respiratory disorders and diseases, a significant worldwide health challenge, are responsible for more than 10% of all disability-adjusted life year (DALYs): a metric used in public health and health impact assessment that estimates the number of years of healthy life lost due to ill-health, disability or early death [62, 63]. Mortality, disability, and morbidity caused by respiratory diseases [12], which are second only to cardiovascular diseases [64], imposed immense economic costs and health burden worldwide. Among respiratory diseases, chronic obstructive pulmonary disease (COPD) and asthma predominantly contribute to the burden. An estimated 65 million people have moderate to severe COPD, of which about 3 million die each year, making it the third leading cause of death worldwide, and the frequency of the disease remains increasing trajectory [65, 66]. About 334 million people have asthma, which is the most common chronic disease of childhood, affecting 14% of children globally. The prevalence of asthma in children keeps rising [67]. Alternatively, sleep-disordered breathing is a less well-quantified respiratory disorder, and more than 100 million people are suffering from it [66].

Characteristics of respiratory disorders and diseases suggest continuous monitoring of respiratory behaviors benefit patients. COPD and asthma, the two most common respiratory diseases, are characterized by airway inflammation, which causes breathlessness in terms of an extrinsic failure of the chest wall to obtain and maintain sufficient lung volume. However, symptoms of the changeability on COPD and asthma have been studied and described as time-dependent, even over one day [68]; thus it is challenging to generalize the characteristics of respiratory behaviors. The diagnosis of respiratory diseases is based on the history of patients, symptoms, and the outcome of attempted therapies. Therefore, the continuous monitoring of the respiratory behaviors offers valuable information to the pre-diagnosis by extracting the clinically relevant parameters to describe the progression of patients' respiratory conditions.

As a physiological activity, respiration is a systematic result of the nonlinear motion of the chest wall and the diaphragm, corresponding to the chest respiration and abdominal respiration, respectively. During inspiration, the expansion of the chest wall and the contraction of the diaphragm pull air into the lung. With further movement of the diaphragm, the content in the abdomen was pulled outward, increasing the circumference of the abdominal wall; whereas in expiration, the chest wall and diaphragm relax and passively restore to their anatomic positions, which pushes air out of the lung resulting in the circumferences of the chest and abdominal walls to decrease.

Several research groups have reported various respiration monitoring methods. For example, bands with sensors embedded or fiber-optic based strain gauges around the chest wall were used to detect chest wall perimeter change caused by respiration [69]. Inertial sensors or polyvinylidene-fluoride (PVDF) polymer-based piezoelectric transducers that were directly attached to the human chest to detect the pulsatile vibration due to the respiration [70, 71]. In other studies, strain sensors made of different materials, including graphene [72], carbon nanotubes [73], and carbonized silk fabric [74], were attached to the human chest to measure local strain realizing the respiration monitoring.

However, all those methods fail to monitor systematic breathing motion and are limited to produce respiratory rate, which has minimal clinical value [47]. Optoelectronic plethysmography (OEP) offers readily available clinically valid information of respiratory monitoring, yet requires multiple external cameras to monitor the location of markers on the body to evaluate the respiration [75]. Inertial measurement unit (IMU) and strain sensors were attached to the abdomen and chest to monitor respiratory behaviors simultaneously when the subjects are in a standing posture [76, 77]; however, the non-optimal wear-ability or/and the potential monitoring failure caused by inductance plethysmography (RIP) belt slippage as well as the respiratory monitoring in a single posture may not be realistic or helpful for continuous monitoring. Unique skin-mounted soft electronics were recently reported to detect the human motions toward motion recognition [78, 79]. Our wireless sensor is a stand-alone system, with no need for any specific external settings, thus allowing ubiquitous respiratory monitoring, e.g., home. Postures have a non-negligible influence on respiratory behaviors. The body postures affect the anatomical dimensions of the upper airway, which may become impaired in specific postures. Particularly during sleep with a lower consciousness, the collapsibility of upper airways has been identified as an important pathogenic factor in obstructive sleep apnea (OSA) [80-82]. Further, respiratory behaviors are a function of the differences in the anatomy of the abdominal muscles and the influence of gravity caused by postures change [83]. Posture-related instability of the human airway and anatomy structures may have serious medical implications, yet few reports exist on a wearable respiratory monitoring system to analyze individuals' respiratory behaviors at various postures, contributing meaningful, relevant clinical values.

This work presents a stand-alone wireless sensors system, equipped with a machine learning algorithm, that offers continuous measurement of respiratory behaviors. The system extracts and classifies key features of individuals' respiratory behaviors at different postures to study individual- and posture-dependent respiratory behaviors.

3.2. Material and Method

3.2.1. Wireless wearable sensor

The localized circumference changes of the chest and abdominal walls are the respiration's external appearance and can effectively emulate the lung volume change during respiration [84-87]. We used two wireless wearable sensors: one (Sensor1) was placed 1 cm above the umbilicus for abdominal respiration [7], and the other one (Sensor2) was placed on the midway between the xiphoid process and the costal margin for chest respiration, as shown in Fig. 3.1A., which has been validated by our previous work [88].

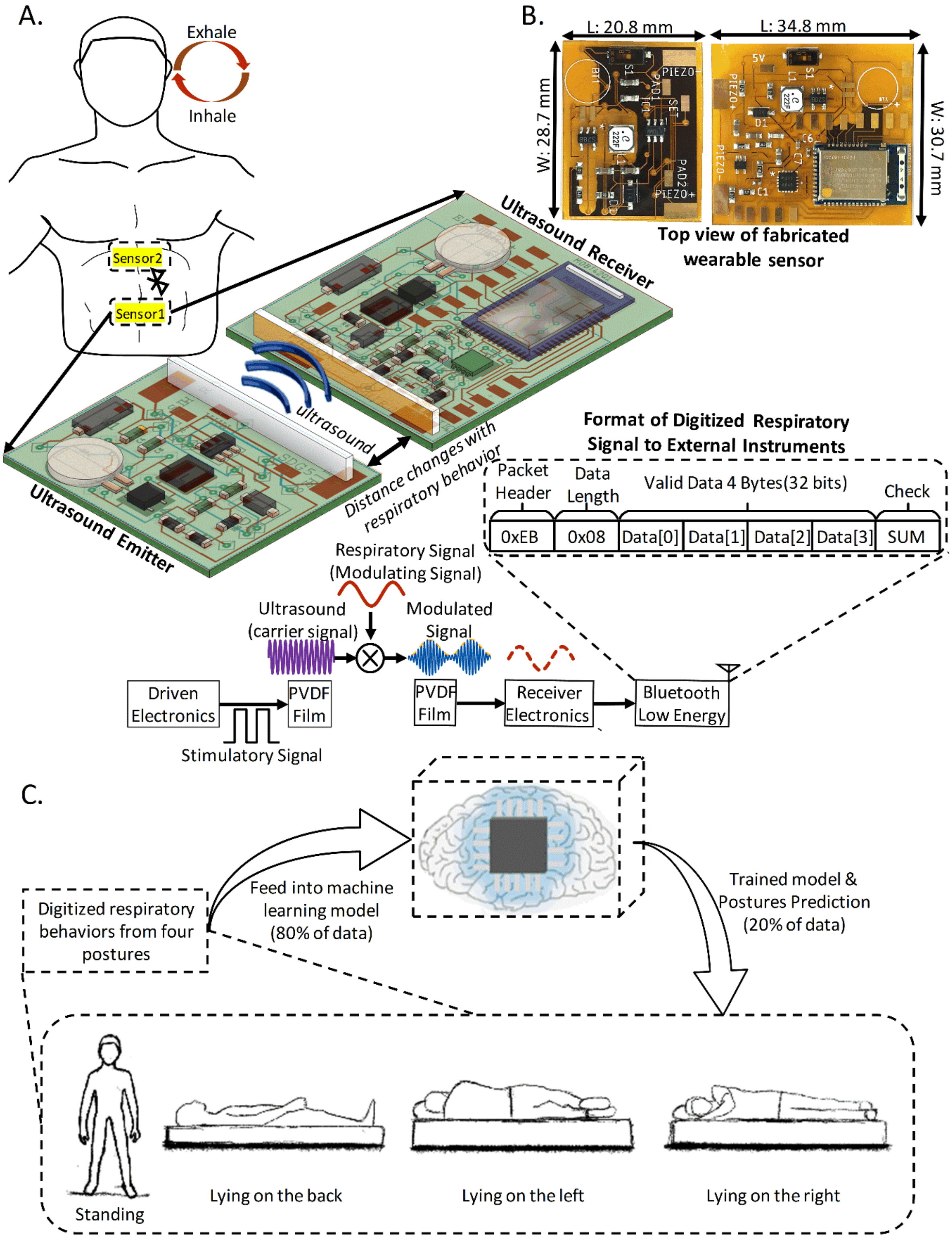

Figure 3.1. System Overview (A) wireless wearable sensors attached on the midway of the xiphoid process and the costal margin, one on each location, corresponding to the

abdomen-apposed rib cage, and 1 cm above the umbilicus, respectively. The wearable sensors convert the local strain, by measuring the attenuation in ultrasound as a function of the distance between the emitter and the receiver, to lung volume. The respiratory behaviors signal was amplified and extracted by onboard electronics and wirelessly transmitted to an external machine. (B) Photo of the top view of the fabricated wireless wearable sensor on a flexible polyimide substrate with a footprint of 30.7×55.6×3 mm^3. (C) Respiratory behaviors data collected from four postures of subjects were fed into a machine learning algorithm. Among the data, 80% were used to train the random forest classifier, and the remaining 20% was used to be the test dataset to predict the respiratory postures based on the extracted features.

The wireless wearable sensor is composed of an emitter to radiate ultrasound and a receiver to receive the distance-elapsed attenuated ultrasound. The two parts of the wearable sensor move further apart during the inspiration due to the increase in the circumference of the chest and abdominal walls, which results in a more attenuated ultrasound signal. In contrast, during expiration, the two parts move closer, resulting in a stronger received ultrasound signal. A non-polarized pulse stimulatory signal at 50 kHz is applied across the PVDF film to generate ultrasound. The respiratory signal modulates the emitted ultrasound carrier, which is received by another PVDF receiver that converts the mechanical signal to an electrical signal. After demodulation and amplification, the respiratory signal is extracted by an envelope detector, and the onboard Bluetooth module (MDBT40Q) wirelessly transmits the digitized respiratory signal to an external machine for data analysis, e.g., a laptop, that had custom-made data collecting program (appendix G, the interface of tailor-made data collecting program). Fig. 3.1A illustrates a simplified process, while more details of electronics and schematic used in the wearable sensor follow in appendix H. The wearable sensor was fabricated on a flexible 0.1 mm-thick polyimide substrate (PCBWay), as shown in Fig. 3.1B. The wearable sensor occupied

$55.6 \times 30.7 \times 3$ mm^3 and weighed 5.5 g, including two 1.6 g button cell batteries. Fig. 3.1C shows a simplified conceptual process.

3.2.2. Study Design

We recruited eleven subjects to attach the wireless wearable sensors on the midway between the xiphoid process and the costal margin, corresponding to the abdomen-apposed rib cage, and 1 cm above the umbilicus to collect respiratory behaviors within four postures. All participants provided informed consent, and this study was approved by the Arizona State University (ASU) Institutional Review Board (IRB).

Eligibility, inclusion, and exclusion criteria for subject recruitment: convenience sample from healthy adults (18 years or older) who responded to the recruitment flyer. Subjects who smoke or have a family history of respiratory diseases were excluded from the study. In total, eleven subjects were included in the study.

For each subject, the signals coming from the two wireless wearable sensors were organized into a series of segmented, Gaussian-filtered data with a moving window size of 100 data points, with the sliding scale of 20 data points. This data transformation was separately performed for the raw data stream received from two wearable sensors on the chest and abdomen and repeated for the four postures. From each data segment, summary features, i.e., mean and variance, filtered data themselves, the first and second differential of the data, and the wavelet coefficients were extracted.

Characterized by its ability to reduce overfitting problems and rank the importance of classification variables naturally, the random forest classifier has been widely used in machine-learning applications. It is an algorithm for classification based on the bagging algorithm and uses an ensemble learning technique. We used the random forest classifier in the sci-kit-learn package (Python 3.6) and determined 200 decision trees in the finalized random forest classifier. To build a prediction classifier for the subject posture, the feature sets, subject posture information, and other relevant information were entered into a random forest classifier. In general, the training/test set was split into an 80/20 ratio, using 80% of data for training and 20% for testing. The classifier produced multinomial probability models for the four postures. The posture assigned with the highest probability was selected as the predicted value and compared against the actual posture. The proportion of the correct classification was calculated for each run to assess the random forest classifier's performance.

We constructed three separate prediction classifiers: the generic, individual, and the weighted-adaptive classifiers. For the generic classifier, the entirety of the feature sets from a small number of subjects at a time was used to construct the classifier and used to predict the outcome of the subject not included in the classifier building step. The predicted values were compared against the actual subject postures. The generic classifier's performance was assessed across all 120 possible combinations that arise from choosing three subjects out of ten (excluding one subject for test purpose). The individual classifier was applied separately for each subject, using only the feature sets and/or sensors relevant to the particular subject. This created multiple prediction classifiers for each subject. The overall classification performance was assessed by computing the average performance across the individual prediction outcomes. We also considered a weighted-adaptive classifier that is a weighted probability of the generic and individual classifiers' multinomial probabilities to explore how to keep accuracy and improve applicability. We used the randomly resampled data from the same individual to construct the equal number of predictive multinomial distributions from random forest classifier to compute weighted probabilities of finding the final predicted accuracy.

3.2.3. Respiratory Behaviors Collecting Protocol

Eleven subjects were included in this study. To better illustrate the respiratory behaviors, subjects were tested in quiet breathing [89]. Each subject wearing two wireless wearable sensors attached to selected locations performed quiet breathing on the following four postures: standing, lying on the back, lying on the left, and lying on the right.

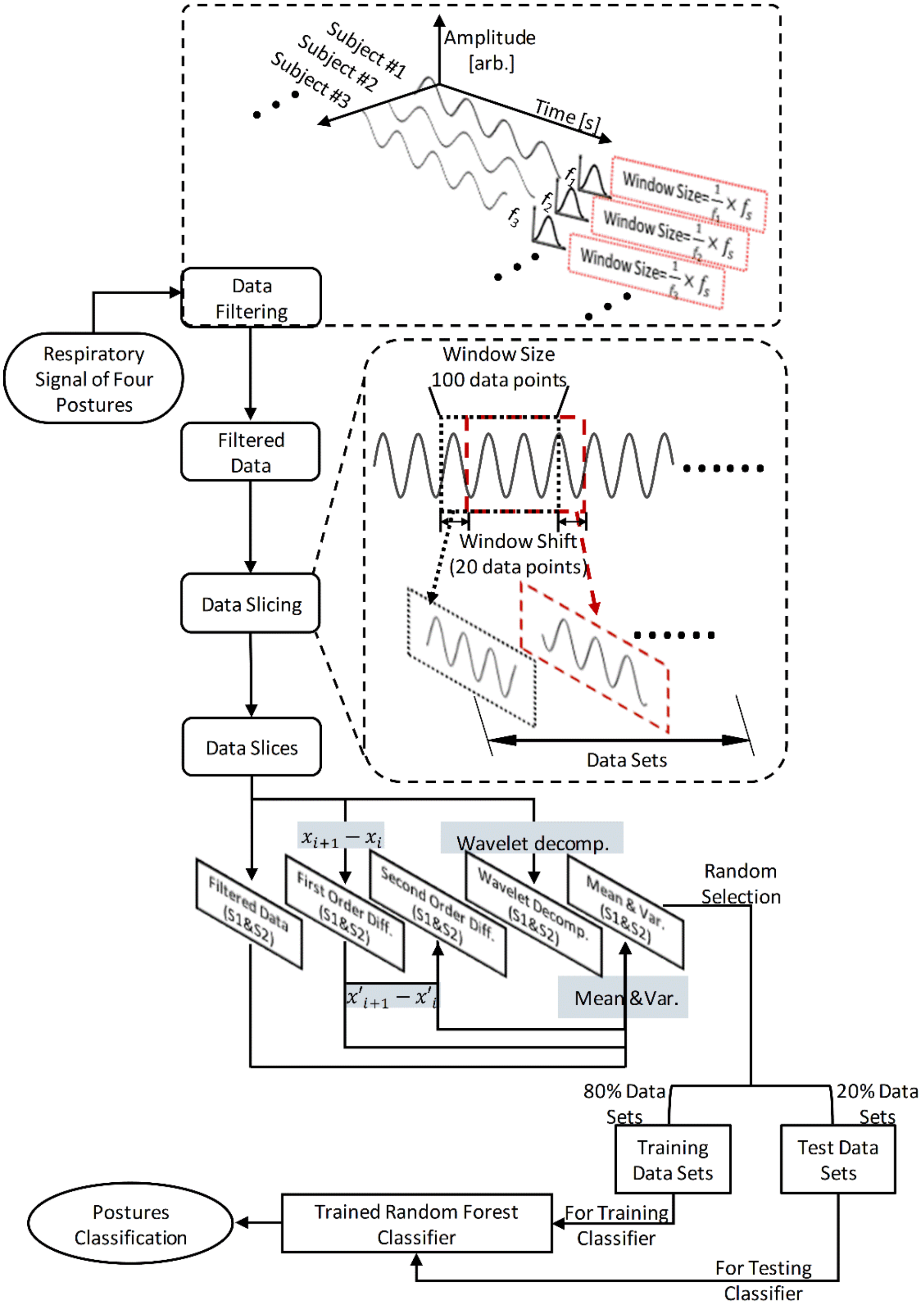

Figure 3.2. Machine Learning Algorithm Process Flow. Respiratory signals collected from subjects using two wireless wearable sensors were fed into the Gaussian filters with respiratory rate-dependent windows size. After filtering, respiration signals were sliced by a 100 data points wide window. The slicing window shifts with a step of 20 data points resulting in 300 slices for a given posture and 1200 slices in total for four postures per individual. Upon the preparation of the data sets, 80% of them were used to train the

random forest classifier, and 20% were used to test the classifier. Features extraction were performed in the following order: filtered respiration signal (Sensor1 or/and Sensor2), fist order differential (Sensor1 or/and Sensor2), second-order differential (Sensor1 or/and Sensor2), mean values with variances (Sensor1 or/and Sensor2). Resulting features of training data sets (80% of data) were used to train the random forest classifiers, followed by accuracy testing using the well-built random forest classifier on the remaining test data sets (20% of data), resulting in the final prediction of respiratory behaviors posture.

3.2.4. Three Cases to Monitor Respiratory Behaviors

For a given posture, we collected 10 minutes of respiratory behaviors wirelessly using two wearable sensors with a sampling frequency of 10 Hz. A healthy adult has a respiratory rate within the range of 12 to 18 respiratory cycles per minute [90], corresponding to 30 to 50 data points per respiratory cycle at a sampling frequency of 10 Hz. This repetitive nature becomes very attractive to train machine learning algorithms. We evaluated the efficacy of using one or/and two wearable sensors in postures classification by using machine learning algorithms. Three cases: the abdominal respiration only (Sensor1), the chest respiration only (Sensor2), and both the abdominal and chest respiration (Sensor1 & Sensor2). Fig. 3.2 shows the process flow of the collected data. It started with the Gaussian window filtering data with respiratory rate-dependent window size (more details of the Gaussian filter window size are in appendix I). This was followed by the data slicing using a window size of 100 data points, approximately covering two respiratory periods. With a sliding scale of 20 data points, we obtained 300 slices at one given posture and 1200 slices in total for four postures per subject. The processed data were used to extract multiple features, including mean and variance, filtered data themselves, the first and second differential of the data, and the wavelet decompositions. 80% of features were chronologically selected for training the random forest classifier, and the remaining 20% were used as test data for evaluating the trained classifier.

3.3. Results and Discussion

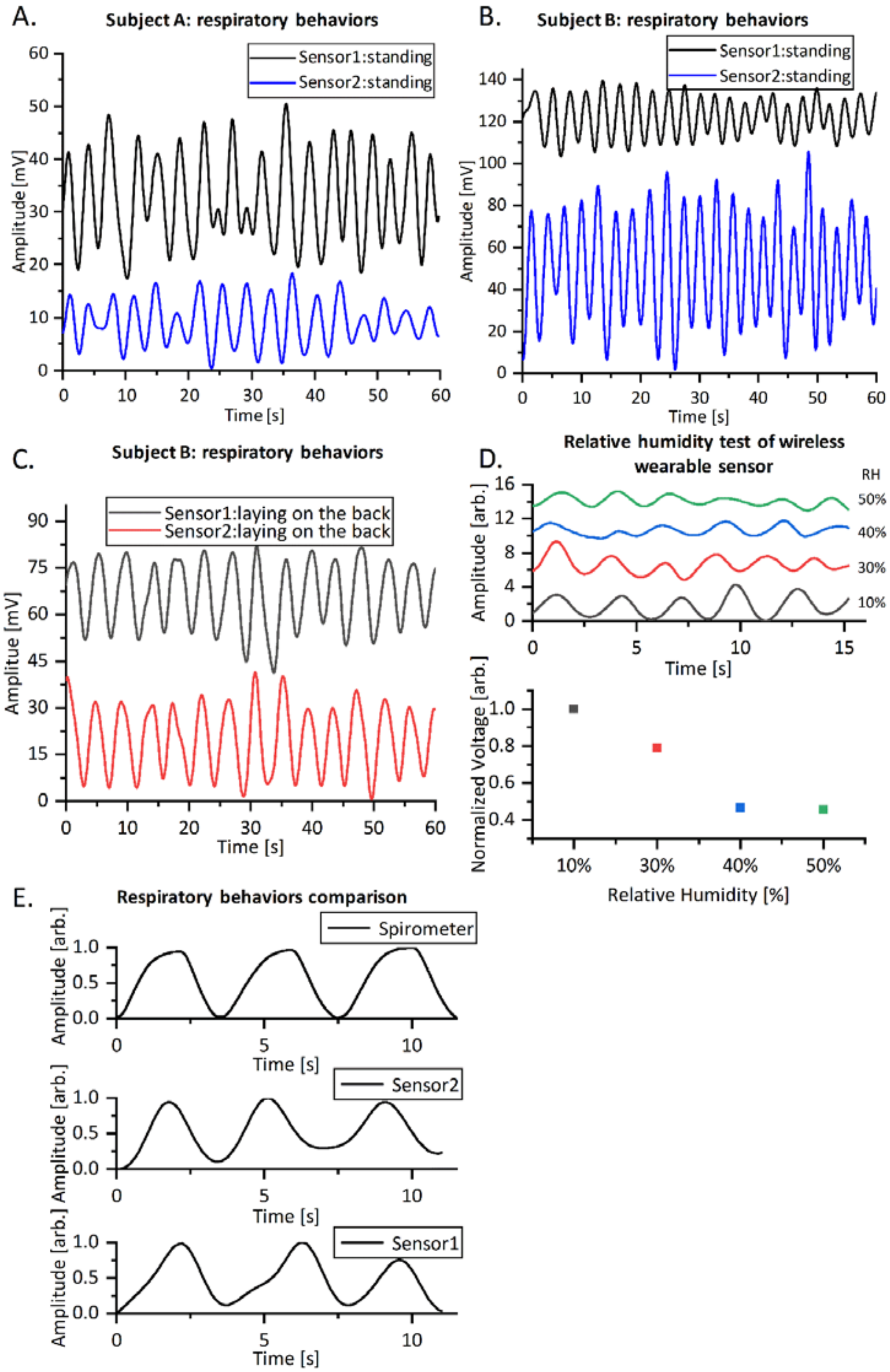

Figure 3.3. Wearable System Verification in Practical Settings. (A) Temporal data collected from the abdominal (Sensor1) and the chest (Sensor2) walls of subject A in standing posture, who is a primarily abdominal breather, and (B) those from subject B, who is a primary chest breather. (C) data from subject B (chest breather) at a different posture (lying on the back). The amplitude change of Sensor1 is more significant than that of Sensor 2, suggesting subject B shows primarily abdominal respiration when lying on the back. (D) The relative humidity levels test of the wireless wearable sensor. With the relative, peak to peak amplitudes of the respiratory behaviors decrease when humidity increases from 10% to 50%, as expected due to the attenuation of ultrasound in the air as a function of humidity. (E) The comparison of the normalized respiratory behaviors collected by Sensor1, Sensor2, and Spirometer.

3.3.1. Wireless Acquisition of Respiratory Signals Using the Wireless Sensor System

Subject A, abdominal breather, wearing the wireless sensor in standing posture, performed the quiet breathing. Sensor1 (abdominal respiration) produces lager amplitude change than Sensor2 (chest respiration) does for subject A (Fig. 3.3A): the abdominal respiration contributes more than the chest respiration. Subject B, chest breather, showed the opposite (Fig. 3.3B): a smaller amplitude change from Sensor1 than that from Sensor2, translating subject B has a primarily chest respiration. On the other hand, respiratory behaviors may change as a function of postures. During quiet breathing, Fig. 3.3C shows subject B is an abdominal breather when supine and a chest breather when upright [91].

3.3.2. Verification of the Wireless Wearable Sensor in a Practical Setting

In our previous work[88], the wireless wearable sensor was tested on the surface of different curvatures, at different rotation angles, under different temperatures, and characterized by dynamic tests including walking and running with a speed of 1.2 and 2 m/s for 20 seconds. Besides, the wireless wearable sensor was tested as a function of relative humidity levels, in the range of 10%-50%, covering the human comfort zone of relative humidity levels in daily life, which is lower than 60% and higher than 25% (Fig. 3.3D) [92]. The amplitude of the sensor decreases as the humidity increases, as expected, as the ultrasound's attenuation increases in the air [93]. The amplitude of sensors changes as a function of humidity, yet the inhale/exhale cycle, e.g., average 15 times a minute, occurs significantly faster than the humidity change of daily life. Thus, the wirelessly collected data may be treated insensitively to humidity change at the time of acquisition. The temporal outputs of Sensor1 and Sensor2 were collected simultaneously along with a spirometer (Pneumotrac Spirometer, Model 6800, Vitalograph Inc.), as shown in Fig. 3.3E, suggesting that the temporal data of the wireless sensor may be a great source in recognizing the features of respiratory behaviors.

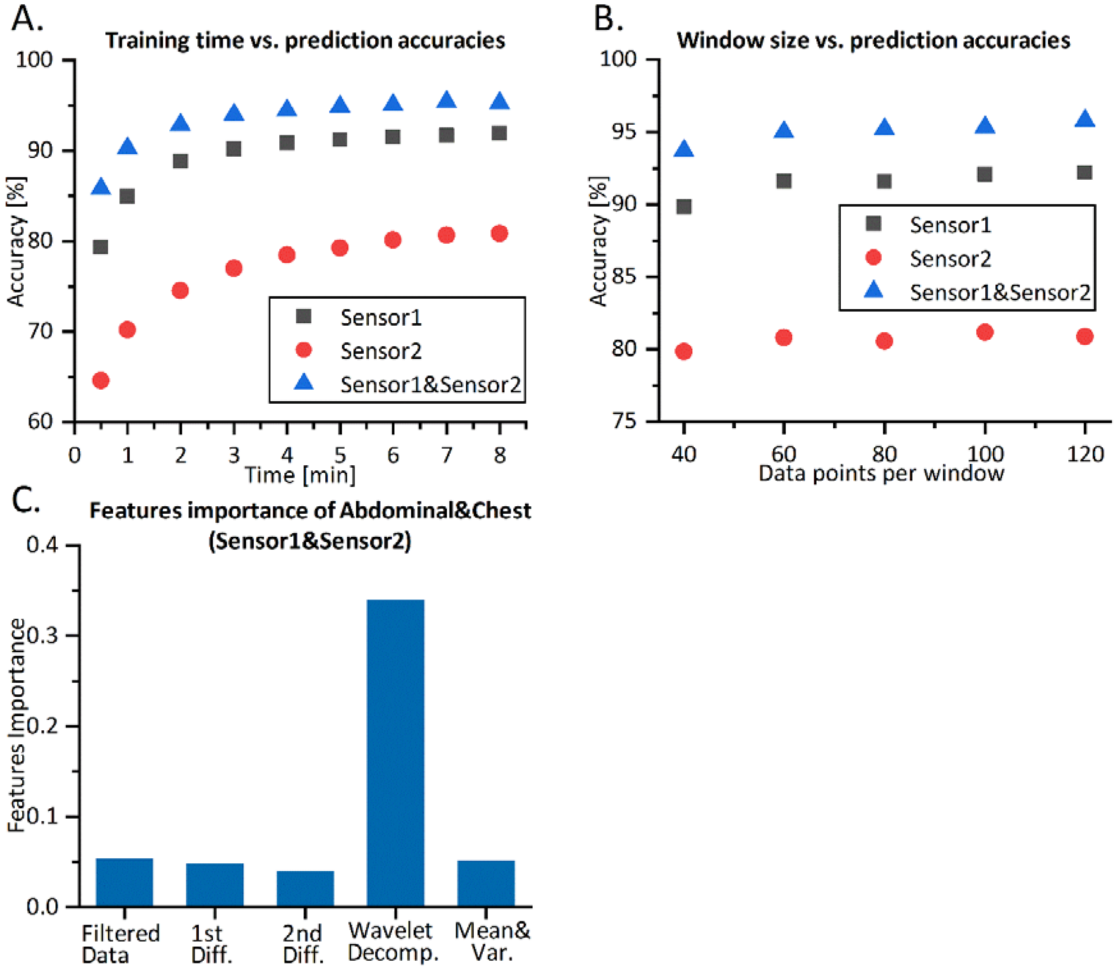

Figure 3.4. Analysis of Optimum Machine-Learning Parameters. (A) Training time optimization. The accuracy of two sensors combined mark higher than those of Sensor1 or Sensor2 alone. The accuracies saturate at 5-6 mins of training, showing the efficacy of repetitive breathing data. (B) Selection of the width of the slicing window. The accuracies mark high at >60 data points per window. (C) The importance order of the extracted features used in the random forest classifiers. The wavelet decomposition dominates over other features, which has a good agreement with the non-stationary, transient, and non-linear characteristics of the respiratory behaviors.

3.3.3. Optimization of Training Time and Window Size

The posture prediction accuracies of Sensor1, Sensor2, and two combined were evaluated as a function of training time (Fig. 3.4A), demonstrating a stable and accurate trained random forest classifier after 6 minutes, approximately 4800 data points. Fig. 3.4B illustrates the accuracies as a function of window sizes. The accuracies are rather independent of window sizes within 60 to 100 data points per window. We chose 100 data points per window to meet the tradeoff between the accuracies and a large number of data slices for training. The random forest classifier trained by the two sensors combined offers higher accuracy than that of Sensor1 or Sensor2 alone, regardless of the training time and window size, highly suggesting the data from two sensors monitor the respiratory behaviors more entirely and more accurately.

3.3.4. Wavelet Decomposition Analysis

Fig. 3.4C shows the importance ranking of extracted respiratory features Sensor1 and Sensor2. The wavelet decomposition predominantly contributes to the final prediction in a random forest classifier. Feature importance rankings of abdominal respiration only (Sensor1) and chest respiration only (Sensor2) are in appendix J. Featured by the strengths of the capability of analyzing transient, non-stationary signals, like respiratory signals [94] as well as time-frequency analysis [95], the wavelet decomposition shows strong relevance in both time and frequency domains for extracting more details of respiratory features for classifier training.

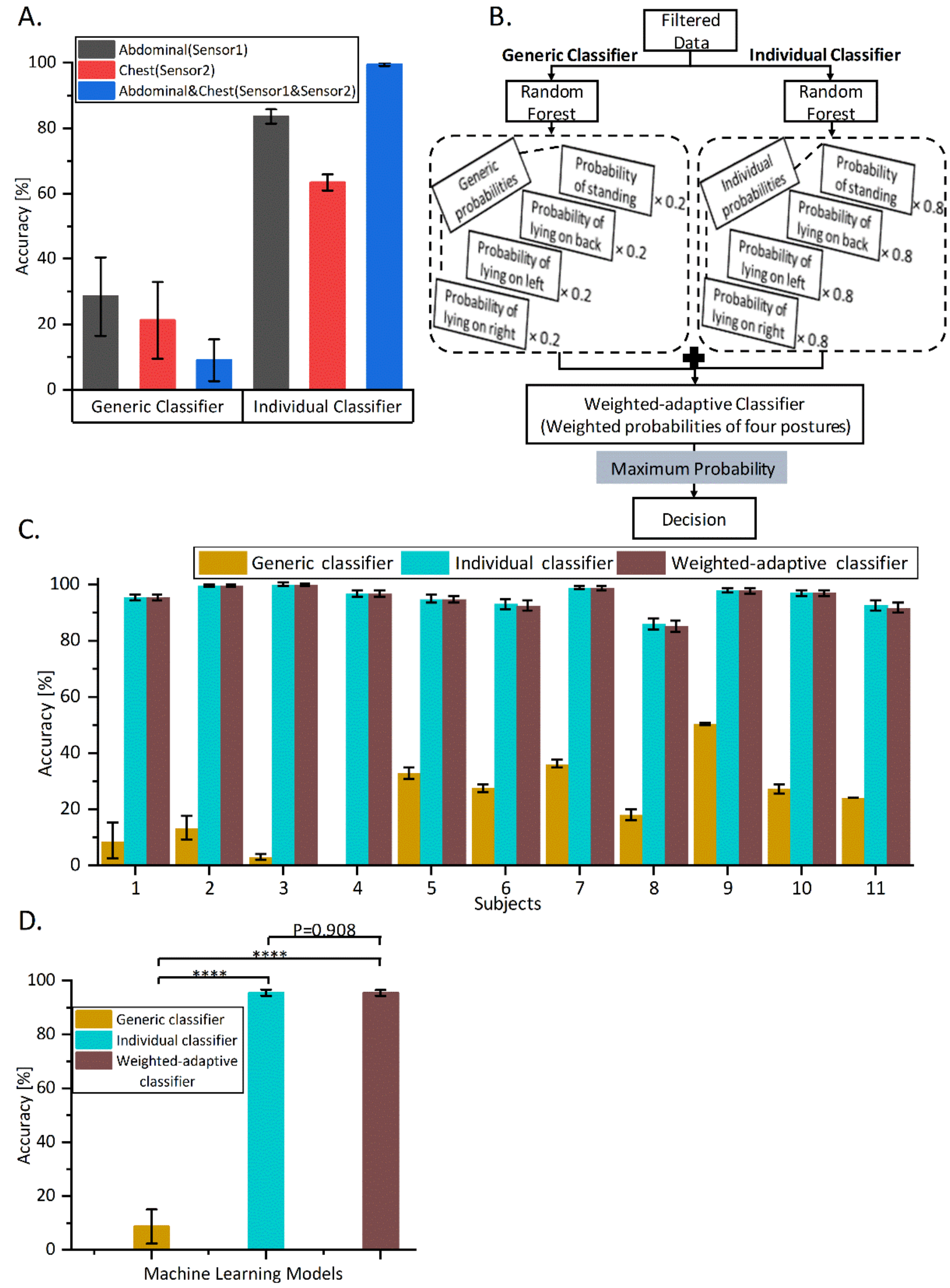

Figure 3.5. Three Random Forest Classifiers Results Summary and Statistical Analysis. (A) Comparison between the generic classifier and the individual classifier. Generic classifier, a classifier combing all the features of respiratory behaviors of all the subjects together, marks poor capability to distinguish the differences of the respiratory

behaviors within different postures for all three cases: Sensor1, Sensor2, and Sensor1 & Sensor2; whereas the individual classifier, a classifier custom-tailored for an individual, shows significantly higher prediction accuracy in recognizing the respiratory features within different postures. (B) The simplified illustration of the weighted-adaptive classifier. The weighted-adaptive classifier is comprised of 80% of the individual classifier and 20% generic classifier, taking advantage of both broad applicability and high accuracy. (C) The accuracies of generic, individual, and weighted-adaptive classifiers on all eleven subjects. All eleven subjects show the lowest accuracy on the generic classifier and considerably high accuracies on individual and weight-adaptive classifiers. (D) The significance analysis of the generic, individual, and weight-adapted classifiers: the accuracies of predicting the postures of subjects based on collected respiratory data. The individual and weighted-adaptive classifiers show significantly higher accuracies over the generic classifier(****P<0.0001) and mark almost equivalent accuracies (P=0.908) between the two classifiers.

3.3.5. Three Random Forest Classifiers

We developed and evaluated three random forest classifiers, including generic, individual, and weighted-adaptive classifiers, to study the individuality of the respiratory behaviors of eleven subjects.

The generic classifier offers a one-fits-all classifier to extract the common characteristics of subjects. We built the generic classifier of three, five, seven, and nine subjects, and the prediction accuracies decrease as the number of subjects included in the classifier increases. Thus, the generic classifier of three subjects is chosen for the comparison throughout this work. More details are shown in appendix K. The generic classifier executed all possible 120 combinations, $C_{10}^{3} = 120$ (three out of ten subjects (excluding one subject for testing purpose)). The generic classifier's accuracy is low, < 40% (Fig. 3.5A), as expected, because of highly significant individuality in respiratory behaviors. Furthermore, the chest and abdominal respiration are systematic, yet are different on extracted respiratory features due to the nonlinear motion of the chest and abdominal walls. These suggest the generic classifier may not be suitable to capture the various respiratory behaviors within four postures of subjects.

The individual classifier uses 80% data for training and 20% data for testing from each individual. The individual classifier marks significantly higher accuracies than those of the generic classifier, 83.56±2.15%, 63.35±2.46%, and 99.53±0.04%, respectively, on abdominal respiration only (Sensor1), chest respiration only (Sensor2), and from both abdominal and chest respiration (Sensor1&Sensor2) shown in Fig. 3.5A. In particular, Sensor1 & Sensor2, the individual classifier using both chest and abdominal respiratory data, yields higher accuracy than Sensor1 or Sensor2 alone by 19.1% and 57.1%, respectively, supporting using both sensors can trace and translate the systematic respiratory behaviors more accurately.

The individual classifier of Sensor1 and Sensor2 marks very high accuracy to predict posture-dependent individual-dependent respiratory behaviors. A limitation exists, however, on the individual model: narrow applicability. To address the limitations of a single classifier, multiple classifiers are lumped together to aggregate the predictions of individual classifiers [96-99]. We introduce a weighted-adaptive classifier, a weighted probability of 20% probability from the generic classifier and 80% probability from the individual classifier at a given posture (Details of weight selection follows in appendix L). The maximum probability among four weighted probabilities, corresponding to four postures, determines the final classification decision (Fig. 3.5B). A two-tailed t-test performed the evaluation of weighted-adaptive classifier with a null hypothesis of the prediction accuracy of the weighted-adaptive classifier equal to those of individual classifier. P=0.908 in Fig. 3.5D indicates strong evidence to accept the null hypothesis.

The weighted-adaptive and individual classifiers show significantly high prediction accuracies over that of the generic classifier, verified by $P<0.0001$ in Fig. 3.5D. For an individual, the individual classifier performs optimally to describe the individuality of respiratory behaviors. Alternatively, the weighted-adaptive classifier may be attractive, as being featured by the competitive prediction accuracy and better applicability. A summary of eleven subjects' prediction accuracy using the respiratory features from both the chest and abdominal respiration of three origins is shown in Fig. 3.5C. Despite the small number of subjects, the prediction accuracies show consistency across all eleven subjects and demonstrate the accurate tracing capabilities of the two wireless wearable sensors monitoring the systematic respiratory behaviors in order to contribute to respiratory disease management.

3.4. Conclusion

We report a wireless wearable sensors system enhanced by a machine-learning algorithm, capable of monitoring the individuality of the respiratory behaviors via postures classification method. Eleven subjects were included in this study; the number of subjects is relatively small but similar to the sample size of other studies, for examples, respiration mechanism, and respiration-related disease explorations, which have drawn significant clinically-meaningful results [57, 82, 83, 100-103], exploring respiration monitoring by wearable sensors recruited only one subject and tested with a single posture [2, 72, 74, 104, 105].

Several future works may improve our current study. Due to the small number of and rather homogeneous nature of the study subjects, the applicability and generalizability of the study findings to a broader population are unknown at this point.

Diversifying the subjects pool, i.e., by including the elderly and the youth, and healthy and unhealthy subjects will enhance the wireless wearable sensor's applicability and performance with a machine learning algorithm.

Secondly, the generic classifier we explored showed low accuracy for predicting the posture of the subjects. We surmise that it may be due to the individuality of highly individual-dependent respiratory behaviors that were not included in the feature set used to train the classifier, such as demographics. Hence incorporation of the inherent individuality helps us to develop a more accurate generic model.

For an individual, the individual classifier is the ideal option due to its most substantial ability to detect different respiratory behaviors. The apparent weakness of the individual classifier is the generalizability. The prediction classifier constructed from one subject's data does not produce usable guidance for the next subject.

The alternative weighted-adaptive classifier, taking advantage of broad applicability and higher accuracy, addresses the weak applicability of the individual classifier, opening the potential of the applicability to a large group of people to accurately study respiratory behaviors contributing to the diagnosis and control of respiratory diseases. The weighted-adaptive classifier is still dependent on the individual classifier (80% weight); thus, it inherits a similar generalizability weakness.

However, the loss of the generalizability may not be a significant limiting factor in some applications. A predictive model's broad applicability is crucial only when one requires a one-size-fits-all classifier that can be used for all people without any modifications. Such an application may have greater appeal in field devices that require quick but fairly good accuracy as a first-line diagnostic tool where the person’s past medical history is entirely unknown, e.g., in emergencies. On the other hand, in the ubiquitous mobile health era, a subject’s respiratory data, recorded by our wearable sensors, could be utilized to construct the custom-tailored individual model. This approach may be more in line with precision medicine.

Some challenges remain for future work. The wireless wearable system has two sensors monitoring and translating the chest and abdominal respiration within quiet breathing. Within daily dynamic breath (respiratory behaviors during activities), additional electronics are necessary on the sensors to be references removing artifacts induced by human activities. Correspondingly, we need a more robust and sophisticated machine-learning algorithm to monitor respiratory behaviors and accurately extract unique features of respiratory behaviors within various human activities in daily life.

REFERENCES

[1] J. Dai *et al.*, "Ultrafast Response Polyelectrolyte Humidity Sensor for Respiration Monitoring," *ACS Applied Materials & Interfaces*, vol. 11, no. 6, pp. 6483-6490, 2019/02/13 2019, doi: 10.1021/acsami.8b18904.

[2] Y. Pang *et al.*, "Wearable humidity sensor based on porous graphene network for respiration monitoring," *Biosens Bioelectron*, vol. 116, pp. 123-129, Sep 30 2018, doi: 10.1016/j.bios.2018.05.038.

[3] A. Agnihotri, "Human body respiration measurement using digital temperature sensor with I2C interface," *International Journal of Scientific and Research Publications*, vol. 3, no. 3, pp. 1-8, 2013.

[4] M. Folke, F. Granstedt, B. Hök, and H. Scheer, "Comparative Provocation Test of Respiratory Monitoring Methods," *Journal of Clinical Monitoring and Computing*, vol. 17, no. 2, pp. 97-103, 2002/02/01 2002, doi: 10.1023/A:1016309913890.

[5] M. Patino, D. T. Redford, T. W. Quigley, M. Mahmoud, C. D. Kurth, and P. Szmuk, "Accuracy of acoustic respiration rate monitoring in pediatric patients," *Pediatric Anesthesia*, vol. 23, no. 12, pp. 1166-1173, 2013, doi: 10.1111/pan.12254.

[6] O. Mimoz, T. Benard, A. Gaucher, D. Frasca, and B. Debaene, "Accuracy of respiratory rate monitoring using a non-invasive acoustic method after general anaesthesia," *BJA: British Journal of Anaesthesia*, vol. 108, no. 5, pp. 872-875, 2012, doi: 10.1093/bja/aer510.

[7] K. P. Cohen *et al.*, "Comparison of impedance and inductance ventilation sensors on adults during breathing, motion, and simulated airway obstruction," *IEEE Trans Biomed Eng*, vol. 44, no. 7, pp. 555-66, Jul 1997, doi: 10.1109/10.594896.

[8] L. M. Nilsson, "Respiration Signals from Photoplethysmography," *Anesthesia & Analgesia*, vol. 117, no. 4, pp. 859-865, 2013, doi: 10.1213/ANE.0b013e31828098b2.

[9] P. Leonard, T. F. Beattie, P. S. Addison, and J. N. Watson, "Standard pulse oximeters can be used to monitor respiratory rate," *Emergency Medicine Journal*, vol. 20, no. 6, p. 524, 2003, doi: 10.1136/emj.20.6.524.

[10] A. Chen, S. Nam, Y.-C. Lai, and J. Chae, "Low-voltage shock-mitigated micro-electromechanical systems structure," *Appl Phys Lett*, vol. 110, no. 20, p. 201903, 2017, doi: 10.1063/1.4983645.

[11] "Global Strategy for Asthma Management and Prevention (2018 update)," GLOBAL INITIATIVE FOR ASTHMA, 2018.

[12] R. L. Murphy, Jr., S. K. Holford, and W. C. Knowler, "Visual lung-sound characterization by time-expanded wave-form analysis," *N Engl J Med,* vol. 296, no. 17, pp. 968-71, Apr 28 1977, doi: 10.1056/NEJM197704282961704.

[13] "Childhood asthma," *EUROPEAN LUNG white book*, R. L. John Gibson, Yves Sibille, Bo Lundbäck, Ed., 2018, pp. 126-137.

[14] A. Schneider *et al.*, "Diagnostic accuracy of spirometry in primary care," *BMC pulmonary medicine,* vol. 9, pp. 31-31, 2009, doi: 10.1186/1471-2466-9-31.

[15] C. J. Hunter, C. E. Brightling, G. Woltmann, A. J. Wardlaw, and I. D. Pavord, "A comparison of the validity of different diagnostic tests in adults with asthma," *Chest,* vol. 121, no. 4, pp. 1051-7, Apr 2002, doi: 10.1378/chest.121.4.1051.

[16] M. R. Bye, D. Kerstein, and E. Barsh, "The importance of spirometry in the assessment of childhood asthma," *Am J Dis Child,* vol. 146, no. 8, pp. 977-8, Aug 1992, doi: 10.1001/archpedi.1992.02160200099037.

[17] P. Enright, M. Studnicka, and J. Zielinski, "Spirometry to detect and manage chronic obstructive pulmonary disease and asthma in the primary care setting," in *Lung Function Testing: European Respiratory Monograph*, H. S. R. Gosselink Ed., 2005, pp. 1-14.

[18] D. P. Johns, J. A. Walters, and E. H. Walters, "Diagnosis and early detection of COPD using spirometry," *J Thorac Dis,* vol. 6, no. 11, pp. 1557-69, Nov 2014, doi: 10.3978/j.issn.2072-1439.2014.08.18.

[19] S. M. Ching *et al.*, "Detection of airflow limitation using a handheld spirometer in a primary care setting," *Respirology,* vol. 19, no. 5, pp. 689-93, Jul 2014, doi: 10.1111/resp.12291.

[20] T. A. Barnes and L. Fromer, "Spirometry use: detection of chronic obstructive pulmonary disease in the primary care setting," *Clin Interv Aging,* vol. 6, pp. 47-52, 01/27 2011, doi: 10.2147/CIA.S15164.

[21] P. H. Quanjer *et al.*, "Multi-ethnic reference values for spirometry for the 3-95-yr age range: the global lung function 2012 equations," *Eur Respir J,* vol. 40, no. 6, pp. 1324-43, Dec 2012, doi: 10.1183/09031936.00080312.

[22] J. Malka and J. D. Spahn, "When Cough Wheeze and Shortness of Breath Don't Equal Asthma," (in English), *J Aller Cl Imm-Pract*, vol. 4, no. 1, pp. 179-81; quiz 182-3, Jan-Feb 2016, doi: 10.1016/j.jaip.2015.08.008.

[23] H. Milgrom, R. P. Wood Ii, and D. Ingram, "Respiratory Conditions That Mimic Asthma," (in English), *Immunol Allergy Clin,* vol. 18, no. 1, pp. 113-132, Feb 1998, doi: 10.1016/s0889-8561(05)70351-9.

[24] E. M. Wagner, M. C. Liu, G. G. Weinmann, S. Permutt, and E. R. Bleecker, "Peripheral lung resistance in normal and asthmatic subjects," (in eng), *The American review of respiratory disease,* vol. 141, no. 3, pp. 584-8, Mar 1990, doi: 10.1164/ajrccm/141.3.584.

[25] Y. Yu, L. Ye, Y. Song, Y. Guan, and J. Zang, "Wrinkled nitrile rubber films for stretchable and ultra-sensitive respiration sensors," (in English), *Extreme Mechanics Letters,* vol. 11, pp. 128-136, Feb 2017, doi: 10.1016/j.eml.2016.12.003.

[26] S. Howard, A. Lang, S. Sharples, and D. Shaw, "See I told you I was taking it! - Attitudes of adolescents with asthma towards a device monitoring their inhaler use: Implications for future design," (in English), *Appl Ergon,* vol. 58, pp. 224-237, Jan 2017, doi: 10.1016/j.apergo.2016.06.018.

[27] L. K. Williams *et al.*, "Relationship between adherence to inhaled corticosteroids and poor outcomes among adults with asthma," (in English), *J Allergy Clin Immunol,* vol. 114, no. 6, pp. 1288-93, Dec 2004, doi: 10.1016/j.jaci.2004.09.028.

[28] R. A. Covar, J. D. Spahn, J. R. Murphy, S. J. Szefler, and G. Childhood Asthma Management Program Research, "Progression of asthma measured by lung function in the childhood asthma management program," *Am J Respir Crit Care Med,* vol. 170, no. 3, pp. 234-41, Aug 1 2004, doi: 10.1164/rccm.200308-1174OC.

[29] P. M. Gustafsson, L. Watson, K. J. Davis, and K. F. Rabe, "Poor asthma control in children: evidence from epidemiological surveys and implications for clinical practice," *Int J Clin Pract,* vol. 60, no. 3, pp. 321-34, Mar 2006, doi: 10.1111/j.1368-5031.2006.00798.x.

[30] J. M. Foster *et al.*, "Inhaler reminders improve adherence with controller treatment in primary care patients with asthma," *J Allergy Clin Immunol,* vol. 134, no. 6, pp. 1260-1268 e3, Dec 2014, doi: 10.1016/j.jaci.2014.05.041.

[31] T. Charles, D. Quinn, M. Weatherall, S. Aldington, R. Beasley, and S. Holt, "An audiovisual reminder function improves adherence with inhaled corticosteroid therapy in asthma," *J Allergy Clin Immunol,* vol. 119, no. 4, pp. 811-6, Apr 2007, doi: 10.1016/j.jaci.2006.11.700.

[32] J. Gamble, M. Stevenson, and L. G. Heaney, "A study of a multi-level intervention to improve non-adherence in difficult to control asthma," *Respir Med,* vol. 105, no. 9, pp. 1308-15, Sep 2011, doi: 10.1016/j.rmed.2011.03.019.

[33] U. Strandbygaard, S. F. Thomsen, and V. Backer, "A daily SMS reminder increases adherence to asthma treatment: a three-month follow-up study," *Respir Med,* vol. 104, no. 2, pp. 166-71, Feb 2010, doi: 10.1016/j.rmed.2009.10.003.

[34] S. K. Chhabra, "Clinical application of spirometry in asthma: Why, when and how often?," *Lung India*, vol. 32, no. 6, pp. 635-7, Nov-Dec 2015, doi: 10.4103/0970-2113.168139.

[35] B. J. Semmes, M. J. Tobin, J. V. Snyder, and A. Grenvik, "Subjective and objective measurement of tidal volume in critically III patients," *Chest*, vol. 87, no. 5, pp. 577-579, 1985. [Online]. Available: https://www.sciencedirect.com/science/article/pii/S0012369215411729?via%3Dihub.

[36] C. Davis, A. Mazzolini, and D. Murphy, "A new fibre optic sensor for respiratory monitoring," *Australas Phys Eng Sci Med*, vol. 20, no. 4, pp. 214-9, Dec 1997. [Online]. Available: https://www.ncbi.nlm.nih.gov/pubmed/9503693.

[37] I. Eriksson, L. Berggren, and S. Hallgren, "CO2 production and breathing pattern during invasive and non-invasive respiratory monitoring," *Acta Anaesthesiol Scand*, vol. 30, no. 6, pp. 438-43, Aug 1986, doi: 10.1111/j.1399-6576.1986.tb02448.x.

[38] G. Wehrle, P. Nohama, H. J. Kalinowski, P. I. Torres, and L. C. G. Valente, "A fibre optic Bragg grating strain sensor for monitoring ventilatory movements," *Measurement Science and Technology*, vol. 12, no. 7, pp. 805-809, 2001/06/08 2001, doi: 10.1088/0957-0233/12/7/309.

[39] C. Davis, A. Mazzolini, J. Mills, and P. Dargaville, "A new sensor for monitoring chest wall motion during high-frequency oscillatory ventilation," *Med Eng Phys*, vol. 21, no. 9, pp. 619-23, Nov 1999, doi: 10.1016/s1350-4533(99)00094-6.

[40] S. D. Min, D. J. Yoon, S. W. Yoon, Y. H. Yun, and M. Lee, "A study on a non-contacting respiration signal monitoring system using Doppler ultrasound," *Med Biol Eng Comput*, journal article vol. 45, no. 11, pp. 1113-9, Nov 2007, doi: 10.1007/s11517-007-0246-2.

[41] L. Nilsson, A. Johansson, and S. Kalman, "Monitoring of respiratory rate in postoperative care using a new photoplethysmographic technique," (in English), *J Clin Monit Comput*, vol. 16, no. 4, pp. 309-15, 2000, doi: 10.1023/a:1011424732717.

[42] R. E. Barrow, A. J. Vorwald, and E. Domeier, "Capacitance respirometry," *Arch Environ Health*, vol. 19, no. 4, pp. 579-85, Oct 1969, doi: 10.1080/00039896.1969.10666887.

[43] C. I. Franks, B. H. Brown, and D. M. Johnston, "Contactless respiration monitoring of infants," *Med Biol Eng*, vol. 14, no. 3, pp. 306-12, May 1976, doi: 10.1007/BF02478126.

[44] K. Nakajima, T. Tamura, and H. Miike, "Monitoring of heart and respiratory rates by photoplethysmography using a digital filtering technique," (in English), *Med Eng Phys*, vol. 18, no. 5, pp. 365-372, Jul 1996, doi: 10.1016/1350-4533(95)00066-6.

[45] W. Cop, "Methods devices used in ventilatory monitoring," *Encyl. Med. Dev. Instrum*, vol. 4, pp. 2870-2877, 1988.

[46] F. Guder *et al.*, "Paper-Based Electrical Respiration Sensor," *Angew Chem Int Ed Engl*, vol. 55, no. 19, pp. 5727-32, May 4 2016, doi: 10.1002/anie.201511805.

[47] M. Folke, L. Cernerud, M. Ekstrom, and B. Hok, "Critical review of non-invasive respiratory monitoring in medical care," *Med Biol Eng Comput*, journal article vol. 41, no. 4, pp. 377-83, Jul 2003, doi: 10.1007/bf02348078.

[48] W. O. Fenn, "Mechanics of respiration," *Am J Med*, vol. 10, no. 1, pp. 77-90, Jan 1951, doi: 10.1016/0002-9343(51)90221-5.

[49] O. L. Wade, "Movements of the thoracic cage and diaphragm in respiration," *J Physiol*, vol. 124, no. 2, pp. 193-212, May 28 1954, doi: 10.1113/jphysiol.1954.sp005099.

[50] P. Guin and A. Roy, "Design of efficient loadcell for measurement of mechanical impact by piezoelectric PVDF film sensor," *AIP Advances*, vol. 6, no. 9, p. 095122, 2016/09/01 2016, doi: 10.1063/1.4964148.

[51] V. Magori, "Ultrasonic sensors in air," in *1994 Proceedings of IEEE Ultrasonics Symposium*, 31 Oct.-3 Nov. 1994 1994, vol. 1, pp. 471-481 vol.1, doi: 10.1109/ULTSYM.1994.401632.

[52] M. A. O'Reilly and K. Hynynen, "A PVDF receiver for ultrasound monitoring of transcranial focused ultrasound therapy," *IEEE Trans Biomed Eng*, vol. 57, no. 9, pp. 2286-94, Sep 2010, doi: 10.1109/TBME.2010.2050483.

[53] G. R. Harris, R. C. Preston, and A. S. Dereggi, "The impact of piezoelectric PVDF on medical ultrasound exposure measurements, standards, and regulations," *IEEE Trans Ultrason Ferroelectr Freq Control*, vol. 47, no. 6, pp. 1321-35, 2000, doi: 10.1109/58.883521.

[54] M. Specialties, "Piezo Film Sensors Technical Manual," *Measurement*, 2013.

[55] N. SPIROMETRY, "NIOSH SPIROMETRY TRAINING GUIDE," 2003.

[56] M. R. Miller *et al.*, "Standardisation of spirometry," *Eur Respir J*, vol. 26, no. 2, pp. 319-38, Aug 2005, doi: 10.1183/09031936.05.00034805.

[57] E. Agostoni, P. Mognoni, G. Torri, and F. Saracino, "Relation between changes of rib cage circumference and lung volume," (in English), *Journal of Applied Physiology,* vol. 20, no. 6, pp. 1179-1186, 1965, doi: 10.1152/jappl.1965.20.6.1179.

[58] J. Dansereau and I. A. Stokes, "Measurements of the three-dimensional shape of the rib cage," *J Biomech,* vol. 21, no. 11, pp. 893-901, 1988/01/01/ 1988, doi: 10.1016/0021-9290(88)90127-3.

[59] M. A. Rea-Ramirez, *Models of conceptual understanding in human respiration and strategies for instruction*. 1998.

[60] S. S. Braman, "The global burden of asthma," *Chest,* vol. 130, no. 1 Suppl, pp. 4S-12S, Jul 2006, doi: 10.1378/chest.130.1_suppl.4S.

[61] M.-H. Seo, H.-H. Yang, K.-W. Choi, J.-S. Lee, and J.-B. Yoon, "A simple breathing rate-sensing method exploiting a temporarily condensed water layer formed on an oxidized surface," (in English), *Appl Phys Lett,* vol. 106, no. 5, p. 053701, Feb 2 2015, doi: 10.1063/1.4906815.

[62] WorldHealthOrganization. "Death and DALY Estimates for 2004 by Cause, https://www.who.int/gho/mortality_burden_disease/daly_rates/text/en/." (accessed.

[63] A. Havelaar, "Methodological choices for calculating the disease burden and cost-of-illness of foodborne zoonoses in European countries," *Network for the Preventnion and Control of Zoonoses, Med-Vet-Net Administration Bureau,* 2007.

[64] N. J. Kassebaum *et al.*, "Global, regional, and national disability-adjusted life-years (DALYs) for 315 diseases and injuries and healthy life expectancy (HALE), 1990–2015: a systematic analysis for the Global Burden of Disease Study 2015," (in English), *The Lancet,* vol. 388, no. 10053, pp. 1603-1658, Oct 8 2016, doi: 10.1016/s0140-6736(16)31460-x.

[65] P. G. Burney, J. Patel, R. Newson, C. Minelli, and M. Naghavi, "Global and regional trends in COPD mortality, 1990-2010," *Eur Respir J,* vol. 45, no. 5, pp. 1239-47, May 2015, doi: 10.1183/09031936.00142414.

[66] *World Health Organization, Global Surveillance, Prevention and Control of Chronic Respiratory Diseases : A Comprehensive Approach,https://www.who.int/gard/publications/GARD%20Book%202007.pdf*.

[67] N. Pearce *et al.*, "Worldwide trends in the prevalence of asthma symptoms: phase III of the International Study of Asthma and Allergies in Childhood (ISAAC)," *Thorax,* vol. 62, no. 9, pp. 758-66, Sep 2007, doi: 10.1136/thx.2006.070169.

[68] R. Kessler *et al.*, "Symptom variability in patients with severe COPD: a pan-European cross-sectional study," *Eur Respir J,* vol. 37, no. 2, pp. 264-72, Feb 2011, doi: 10.1183/09031936.00051110.

[69] M. Krehel, M. Schmid, R. M. Rossi, L. F. Boesel, G. L. Bona, and L. J. Scherer, "An optical fibre-based sensor for respiratory monitoring," (in eng), *Sensors (Basel),* vol. 14, no. 7, pp. 13088-101, Jul 21 2014, doi: 10.3390/s140713088.

[70] I. Mahbub *et al.*, "A Low-Power Wireless Piezoelectric Sensor-Based Respiration Monitoring System Realized in CMOS Process," (in English), *Ieee Sens J,* vol. 17, no. 6, pp. 1858-1864, Mar 15 2017, doi: 10.1109/jsen.2017.2651073.

[71] A. Cesareo, Y. Previtali, E. Biffi, and A. Aliverti, "Assessment of Breathing Parameters Using an Inertial Measurement Unit (IMU)-Based System," (in eng), *Sensors (Basel),* vol. 19, no. 1, Dec 27 2018, doi: 10.3390/s19010088.

[72] J. J. Park, W. J. Hyun, S. C. Mun, Y. T. Park, and O. O. Park, "Highly stretchable and wearable graphene strain sensors with controllable sensitivity for human motion monitoring," (in English), *ACS Appl Mater Interfaces,* Article vol. 7, no. 11, pp. 6317-24, Mar 25 2015, doi: 10.1021/acsami.5b00695.

[73] B. Liang *et al.*, "Ultra-stretchable and highly sensitive strain sensor based on gradient structure carbon nanotubes," *Nanoscale,* vol. 10, no. 28, pp. 13599-13606, Jul 19 2018, doi: 10.1039/c8nr02528b.

[74] C. Wang *et al.*, "Carbonized Silk Fabric for Ultrastretchable, Highly Sensitive, and Wearable Strain Sensors," (in English), *Adv Mater,* Article vol. 28, no. 31, pp. 6640-8, Aug 2016, doi: 10.1002/adma.201601572.

[75] C. Massaroni *et al.*, "Optoelectronic Plethysmography in Clinical Practice and Research: A Review," *Respiration,* vol. 93, no. 5, pp. 339-354, 2017, doi: 10.1159/000462916.

[76] T. Elfaramawy, C. L. Fall, S. Arab, M. Morissette, F. Lellouche, and B. Gosselin, "A Wireless Respiratory Monitoring System Using a Wearable Patch Sensor Network," (in English), *Ieee Sens J,* vol. 19, no. 2, pp. 650-657, Jan 15 2019, doi: 10.1109/jsen.2018.2877617.

[77] M. Chu *et al.*, "Respiration rate and volume measurements using wearable strain sensors," *NPJ Digit Med,* vol. 2, no. 1, p. 8, 2019/02/13 2019, doi: 10.1038/s41746-019-0083-3.

[78] K. Lee *et al.*, "Mechano-acoustic sensing of physiological processes and body motions via a soft wireless device placed at the suprasternal notch," *Nat Biomed Eng,* vol. 4, no. 2, pp. 148-158, Feb 2020, doi: 10.1038/s41551-019-0480-6.

[79] Y. R. Jeong *et al.*, "A skin-attachable, stretchable integrated system based on liquid GaInSn for wireless human motion monitoring with multi-site sensing capabilities," (in English), *NPG Asia Materials,* vol. 9, no. 10, pp. e443-e443, Oct 27 2017, doi: 10.1038/am.2017.189.

[80] P. Safar, L. A. Escarraga, and F. Chang, "Upper airway obstruction in the unconscious patient," *J Appl Physiol,* vol. 14, no. 5, pp. 760-4, Sep 1959, doi: 10.1152/jappl.1959.14.5.760.

[81] D. A. Pevernagie, A. W. Stanson, P. F. Sheedy, 2nd, B. K. Daniels, and J. W. Shepard, Jr., "Effects of body position on the upper airway of patients with obstructive sleep apnea," *Am J Respir Crit Care Med,* vol. 152, no. 1, pp. 179-85, Jul 1995, doi: 10.1164/ajrccm.152.1.7599821.

[82] T. Penzel, M. Moller, H. F. Becker, L. Knaack, and J. H. Peter, "Effect of sleep position and sleep stage on the collapsibility of the upper airways in patients with sleep apnea," *Sleep,* vol. 24, no. 1, pp. 90-5, Feb 1 2001, doi: 10.1093/sleep/24.1.90.

[83] T. Kera and H. Maruyama, "The effect of posture on respiratory activity of the abdominal muscles," *J Physiol Anthropol Appl Human Sci,* vol. 24, no. 4, pp. 259-65, Jul 2005, doi: 10.2114/jpa.24.259.

[84] R. Farre, J. M. Montserrat, and D. Navajas, "Noninvasive monitoring of respiratory mechanics during sleep," *Eur Respir J,* vol. 24, no. 6, pp. 1052-60, Dec 2004, doi: 10.1183/09031936.04.00072304.

[85] J. P. Cantineau, P. Escourrou, R. Sartene, C. Gaultier, and M. Goldman, "Accuracy of respiratory inductive plethysmography during wakefulness and sleep in patients with obstructive sleep apnea," *Chest,* vol. 102, no. 4, pp. 1145-51, Oct 1992, doi: 10.1378/chest.102.4.1145.

[86] N. A. Collop *et al.*, "Clinical Guidelines for the Use of Unattended Portable Monitors in the Diagnosis of Obstructive Sleep Apnea in Adult Patients," (in English), *Journal of Clinical Sleep Medicine*, vol. 3, no. 7, p. 737, 2007. [Online]. Available: <Go to ISI>://WOS:000209776600012.

[87] K. Konno and J. Mead, "Measurement of the separate volume changes of rib cage and abdomen during breathing," *J Appl Physiol,* vol. 22, no. 3, pp. 407-22, Mar 1967, doi: 10.1152/jappl.1967.22.3.407.

[88] A. Chen *et al.*, "Wireless Wearable Ultrasound Sensor on a Paper Substrate to Characterize Respiratory Behavior," *ACS Sens*, vol. 4, no. 4, pp. 944-952, Apr 26 2019, doi: 10.1021/acssensors.9b00043.

[89] T. L. Stedman, *Stedman's Medical Dictionary*, 28, illustrated ed. Lippincott Williams & Wilkins, 2006.

[90] W. F. Ganong, *Review of medical physiology*. Mcgraw-hill, 1995.

[91] J. T. Sharp, N. B. Goldberg, W. S. Druz, and J. Danon, "Relative contributions of rib cage and abdomen to breathing in normal subjects," *J Appl Physiol,* vol. 39, no. 4, pp. 608-18, Oct 1975, doi: 10.1152/jappl.1975.39.4.608.

[92] W. Fincher and M. Boduch, "Standards of human comfort: relative and absolute," 2009.

[93] R. Raišutis, O. Tumsys, and R. Kazys, "Feasibility study of application of ultrasonic method for precise measurement of the long distances in air," 01/02 2020.

[94] Y. Wang and K. C. Veluvolu, "Time-Frequency Analysis of Non-Stationary Biological Signals with Sparse Linear Regression Based Fourier Linear Combiner," (in eng), *Sensors (Basel),* vol. 17, no. 6, p. 1386, Jun 14 2017, doi: 10.3390/s17061386.

[95] K. Keissar, L. R. Davrath, and S. Akselrod, "Coherence analysis between respiration and heart rate variability using continuous wavelet transform," *Philos Trans A Math Phys Eng Sci,* vol. 367, no. 1892, pp. 1393-406, Apr 13 2009, doi: 10.1098/rsta.2008.0273.

[96] V. Kotu and B. Deshpande, "Data Mining Process," in *Predictive Analytics and Data Mining,* V. Kotu and B. Deshpande Eds. Boston: Morgan Kaufmann, 2015, pp. 17-36.

[97] T. G. Dietterich, "Ensemble Methods in Machine Learning," in *Multiple Classifier Systems,* Berlin, Heidelberg, 2000// 2000: Springer Berlin Heidelberg, pp. 1-15.

[98] P. Peng *et al.*, "Unsupervised cross-dataset transfer learning for person re-identification," in *Proceedings of the IEEE conference on computer vision and pattern recognition*, 2016, pp. 1306-1315.

[99] W.-L. Zheng and B.-L. Lu, "Personalizing EEG-based affective models with transfer learning," presented at the Proceedings of the Twenty-Fifth International Joint Conference on Artificial Intelligence, New York, New York, USA, 2016.

[100] A. DeGroote, M. Wantier, G. Cheron, M. Estenne, and M. Paiva, "Chest wall motion during tidal breathing," (in English), *Journal of Applied Physiology,* vol. 83, no. 5, pp. 1531-1537, Nov 1997. [Online]. Available: <Go to ISI>://WOS:A1997YE86700018.

[101] I. Ayappa, R. G. Norman, A. C. Krieger, A. Rosen, L. O'Malley R, and D. M. Rapoport, "Non-Invasive detection of respiratory effort-related arousals (REras) by a nasal cannula/pressure transducer system," (in English), *Sleep,* Article vol. 23, no. 6, pp. 763-71, Sep 15 2000, doi: 10.1093/sleep/23.6.763.

[102] B. Padasdao, E. Shahhaidar, C. Stickley, and O. Boric-Lubecke, "Electromagnetic Biosensing of Tidal Volume," (in English), *Ieee Sens J*, Article vol. 18, no. 15, pp. 6391-6398, Aug 1 2018, doi: 10.1109/jsen.2018.2844178.

[103] E. H. Bergofsky, "Relative Contributions of the Rib Cage and the Diaphragm to Ventilation in Man," *J Appl Physiol*, vol. 19, no. 4, pp. 698-706, Jul 1964, doi: 10.1152/jappl.1964.19.4.698.

[104] Z. Liu *et al.*, "Flexible piezoelectric nanogenerator in wearable self-powered active sensor for respiration and healthcare monitoring," (in English), *Semicond. Sci. Technol.*, Article vol. 32, no. 6, p. 7, Jun 2017, Art no. 064004, doi: 10.1088/1361-6641/aa68d1.

[105] H. Xue *et al.*, "A wearable pyroelectric nanogenerator and self-powered breathing sensor," (in English), *Nano Energy*, vol. 38, pp. 147-154, Aug 2017, doi: 10.1016/j.nanoen.2017.05.056.

[106] R. S. Shawgo, A. C. Richards Grayson, Y. Li, and M. J. Cima, "BioMEMS for drug delivery," (in English), *Current Opinion in Solid State and Materials Science*, vol. 6, no. 4, pp. 329-334, Aug 2002, doi: 10.1016/s1359-0286(02)00032-3.

[107] D. S. Eddy and D. R. Sparks, "Application of MEMS technology in automotive sensors and actuators," *Proceedings of the IEEE*, vol. 86, no. 8, pp. 1747-1755, 1998, doi: 10.1109/5.704280.

[108] L. Soyoon and B. Hyokyung, "Data Allocation in MEMS-based Mobile Storage Devices," *IEEE Transactions on Consumer Electronics*, vol. 52, no. 2, pp. 472-476, 2006, doi: 10.1109/tce.2006.1649667.

[109] R. Oboe, R. Antonello, E. Lasalandra, G. S. Durante, and L. Prandi, "Control of a Z-axis MEMS vibrational gyroscope," *IEEE/ASME Transactions on Mechatronics*, vol. 10, no. 4, pp. 364-370, 2005, doi: 10.1109/TMECH.2005.852437.

[110] F. Hu, J. Yao, C. Qiu, and H. Ren, "A MEMS micromirror driven by electrostatic force," (in English), *J Electrostat*, vol. 68, no. 3, pp. 237-242, Jun 2010, doi: 10.1016/j.elstat.2010.01.005.

[111] R. Hao, T. Fenggang, W. Weimin, and Y. Jun, "An out-of-plane electrostatic actuator based on the lever principle," *Journal of Micromechanics and Microengineering*, vol. 21, no. 4, p. 045019, 2011. [Online]. Available: http://stacks.iop.org/0960-1317/21/i=4/a=045019.

[112] M. I. Younis, F. Alsaleem, and D. Jordy, "The response of clamped–clamped microbeams under mechanical shock," (in English), *International Journal of Non-Linear Mechanics*, vol. 42, no. 4, pp. 643-657, May 2007, doi: 10.1016/j.ijnonlinmec.2007.01.017.

[113] G. X. Li and F. A. Shemansky Jr, "Drop test and analysis on micro-machined structures," *Sensors and Actuators A: Physical*, vol. 85, no. 1–3, pp. 280-286, 8/25/ 2000, doi: http://dx.doi.org/10.1016/S0924-4247(00)00427-1.

[114] V. T. Srikar and S. D. Senturia, "The reliability of microelectromechanical systems (MEMS) in shock environments," *Journal of Microelectromechanical Systems*, vol. 11, no. 3, pp. 206-214, 2002, doi: 10.1109/JMEMS.2002.1007399.

[115] D. M. Tanner *et al.*, "MEMS reliability in shock environments," in *Reliability Physics Symposium, 2000. Proceedings. 38th Annual 2000 IEEE International*, 2000 2000, pp. 129-138, doi: 10.1109/RELPHY.2000.843903.

[116] T. Niels, S. Tonny, J. Henri, L. Rob, and E. Miko, "Stiction in surface micromachining," *Journal of Micromechanics and Microengineering*, vol. 6, no. 4, p. 385, 1996. [Online]. Available: http://stacks.iop.org/0960-1317/6/i=4/a=005.

[117] B. B. Lim, J. P. Yang, S. X. Chen, J. Q. Mou, and Y. Lu, "Shock analysis of MEMS actuator integrated with HGA for operational and non-operational HDD," in *Magnetic Recording Conference, 2002. Digest of the Asia-Pacific*, 27-29 Aug. 2002 2002, pp. WE-WE, doi: 10.1109/APMRC.2002.1037704.

[118] F. Alsaleem, M. I. Younis, and R. Miles, "An Investigation Into the Effect of the PCB Motion on the Dynamic Response of MEMS Devices Under Mechanical Shock Loads," (in English), *J Electron Packaging*, vol. 130, no. 3, pp. 031002-031002-10, Sep 2008, doi: 10.1115/1.2957319.

[119] M. I. Younis, D. Jordy, and J. M. Pitarresi, "Computationally Efficient Approaches to Characterize the Dynamic Response of Microstructures Under Mechanical Shock," *Journal of Microelectromechanical Systems*, vol. 16, no. 3, pp. 628-638, 2007, doi: 10.1109/JMEMS.2007.896701.

[120] S. Subramanian *et al.*, "Vibration and shock reliability of MEMS: modeling and experimental validation," *Journal of Micromechanics and Microengineering*, vol. 21, no. 4, p. 045022, 2011. [Online]. Available: http://stacks.iop.org/0960-1317/21/i=4/a=045022.

[121] C. Yang, B. Zhang, D. Chen, and L. Lin, "Drop-shock dynamic analysis of MEMS/package system," in *Micro Electro Mechanical Systems (MEMS), 2010 IEEE 23rd International Conference on*, 24-28 Jan. 2010 2010, pp. 520-523, doi: 10.1109/MEMSYS.2010.5442450.

[122] L. B. Wilner, "A high performance variable capacitance accelerometer," in *Instrumentation and Measurement Technology Conference, 1988. IMTC-88. Conference Record., 5th IEEE*, 20-22 Apr 1988 1988, pp. 92-95, doi: 10.1109/IMTC.1988.10826.

[123] S. W. Yoon, N. Yazdi, N. C. Perkins, and K. Najafi, "Micromachined integrated shock protection for MEMS," (in English), *Sensors and Actuators A: Physical,* vol. 130-131, pp. 166-175, Aug 14 2006, doi: 10.1016/j.sna.2005.12.032.

[124] M. W. Weber, "Adaptive circuits and methods for reducing vibration or shock induced errors in inertial sensors," ed: Google Patents, 2008.

[125] A. Fruscione *et al.*, "CIAO: Chandra's data analysis system," in *Society of Photo-Optical Instrumentation Engineers (SPIE) Conference Series*, vol. 6270, 2006.

[126] C. Lanza Fde, A. A. de Camargo, L. R. Archija, J. P. Selman, C. Malaguti, and S. Dal Corso, "Chest wall mobility is related to respiratory muscle strength and lung volumes in healthy subjects," *Respir Care,* vol. 58, no. 12, pp. 2107-12, Dec 2013, doi: 10.4187/respcare.02415.

APPENDIX A

COPYRIGHT

This dissertation includes some of my previously published work. The detailed copyright permission is showing as below:

Chapter 1 is partially Reproduced from [Chen, A.; Nam, S.; Lai, Y.-C.; Chae, J., Low-voltage shock-mitigated micro-electromechanical systems structure. Appl Phys Lett **2017,** 110 (20), 201903.], with the permission of AIP Publishing.

Chapter 2 is Reprinted (adapted) with permission from (Chen, A.; Halton, A. J.; Rhoades, R. D.; Booth, J. C.; Shi, X.; Bu, X.; Wu, N.; Chae, J., Wireless Wearable Ultrasound Sensor on a Paper Substrate to Characterize Respiratory Behavior. ACS Sensors **2019,** 4 (4), 944-952.). Copyright (2020) American Chemical Society.

Chapter 3 is reproduced from Ang Chen, Jianwei Zhang, Liangkai Zhao, Rachel Diane Rhoades, Dong-Yun Kim, Ning Wu, Jianming Liang, and Junseok Chae., Machine-learning enabled wireless wearable sensors to study individuality of respiratory behaviors. Biosensors and Bioelectronics, 2020: p. 112799.

APPENDIX B

LOW-VOLTAGE SHOCK-MITIGATED MICRO-ELECTROMECHANICAL SYSTEMS STRUCTURE

MEMS devices have infiltrated many applications, including the emerging field of drug delivery [106], sensors and actuators in the automotive industry [107], such as accelerometers to deploy airbags [108], gyroscopes for stability control of mobile electronics [109], and many others [110, 111]. MEMS devices contribute the core components of these high-tech products used daily. Consequently, the reliability of MEMS devices becomes a critical factor that must be reconciled.

Characterized by their highly miniaturized size and the facile fabrication process, MEMS devices are widely used in multi-physics environments, exposing them to mechanical, thermal, chemical, and other disturbances. Among them, one of the most critical issues affecting the reliability of MEMS devices is the external mechanical shock. An external mechanical shock can be defined as a sudden force over a short period applied on the MEMS device relative to the natural frequency of the structure. It can cause cracking, chipping and fracture due to the highly induced loads on the structure [112], which is a key factor to be considered in the design stage of MEMS devices [113]. MEMS structures are subjected to external mechanical shocks during fabrication, deployment, or operation [114]. In certain situations, a MEMS device can be subjected to an extreme shock-load magnitude of greater than 2×10^4 g (g is the acceleration of gravity, 9.81 m/s^2). If severe enough, it can cause irreversible damage to devices [115]. Without a proper mitigation mechanism, the overall system functionality can be affected by severe deformation of the microstructure [113]. Furthermore, exposure of MEMS structures to dynamic loads due to mechanical shock can also cause mechanical and electrical failures, [112] such as the stiction of micro-beams [116] and short circuit of capacitors [115] respectively. In hard disk drives, an unexpected drop may result in damaging of the MEMS actuator, affecting the bandwidth of servo tracking and fine positioning of magnetic head [117]. Other well-developed portable devices contain MEMS structures, which re-emphasize the requirement for reliability against shock [118].

Investigation into the protection of MEMS devices from external shock has led to multiple findings. Srikar *et al.* explored a theoretical analysis of the reliability of MEMS under shock, evaluating shocks in the form of elastic waves, vibration, and quasi-static oscillation in terms of the overall shock duration [114]. Younis *et al.* reported an efficient computational model of the dynamic response MEMS structures demonstrate under shock [119]. Development of a general method for modeling the reliability of MEMS devices established a reference for the predicted maximum acceleration of vibration and maximum shock based on the frequency and pulse length [120]. Yang *et al.* also dynamically analyzed the drop-shock of MEMS/Package system [121].

While many theoretical and experimental studies of MEMS shock response have been explored, only a small number of prior studies have attempted to mitigate the impact of shock. Wilner *et al.* reported hard shock stops as a mitigation method; however, these physical structures tended to generate secondary impacts and cause undesirable device oscillations [122]. Yoon *et al.* suggested nonlinear springs and soft coatings in order to improve shock mitigation [123]. Weber *et al.* presented adaptive control to reduce vibration-induced bias errors in inertial sensors [124]. These attempts require sophisticated structures and algorithms to implement and are less effective and sensitive upon implementation than structures without shock mitigating features.

To overcome some of these challenges, we present a novel, dual-membrane MEMS structure that can effectively mitigate shock using electrostatic stimuli in conjunction with inherent restoration force. Comparing a conventional MEMS configuration, i.e. a structure with a movable membrane and a fixed substrate (Fig. B.1(a)), with a shock mitigating dual membrane structure (Fig. B.1(b)) allows us to perform a side-by-side analysis of the shock responses of these structures. The dual-membrane structure effectively prevents the movable bottom membrane from traveling beyond the allowed distance by simply adding a second thin-film membrane on top of it. This structure effectively reduces the bottom membrane travel distance by 41.5%, upon deploying merely 0.565 V onto the additional membrane under *ex-situ* control and 56% by applying 1.72 V under *is-situ* dynamic control. Therefore, this shock mitigating technique can be applied throughout the field of MEMS to drastically decrease shock impact on micro-speakers, capacitive actuators, harsh environmental sensors, and other transducers.

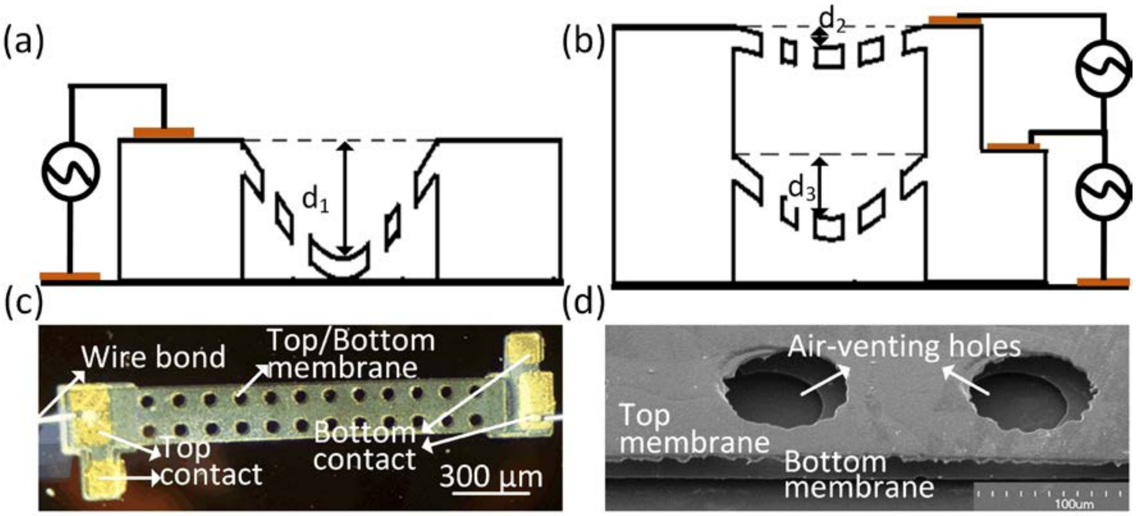

Figure B.1. (a) A conventional single movable membrane upon shock. (b) Dual-membrane structure with an additional top membrane and a movable bottom membrane upon shock. (c) Top view of fabricated dual-membrane device. (d) Cross-section view of fabricated dual-membrane device.

The fabrication process to develop the dual-membrane structure supports CMOS-compatible technology. The first step required a 400-nm-thick silicon nitride layer to be deposited by plasma-enhanced chemical vapor deposition (PECVD) for isolation. To make a silicon substrate contact, a 3 µm silicon nitride layer was removed by fluorine-based reactive-ion etching (RIE) (CF_4: 50sccm, O_2: 5sccm, pressure: 50 mTorr, power:150 W). It was followed by a 4-µm-thick silicon dioxide deposition by PECVD for the first sacrificial layer. The bottom membrane composes of three layers: a 200-nm-thick silicon nitride layer for isolation from the substrate, a 1-µm-thick highly-doped polysilicon, and another 400-nm-thick silicon nitride for the isolation between membranes. We defined the bottom membrane, as well as air-venting holes, using fluorine-based RIE (Si_3N_4/Polysilicon: CF_4: 50/30 sccm, O_2: 5/10 sccm, pressure: 50/175 mTorr, power/RF power: 150/50 W). Then, a 4-µm-thick second sacrificial layer of silicon dioxide, followed by the top membrane, were deposited. The top membrane consists of two layers: 200-nm-thick PECVD silicon nitride and 1-µm-thick low pressure chemical vapor deposition (LPCVD) highly-doped polysilicon. To form the air-venting holes, Fluorine-based RIE was used to etch the top membrane (Polysilicon/Si_3N_4). Thin-film layers of Cr/Au (20/200 nm), form electrical contacts to the top membrane, bottom membrane, and substrate, which are then connected to external readout using wire bond. The dual membranes are free to move once the two sacrificial layers were etched by a 10% hydrofluoric acid solution. Fig. B.1(c) and B.1(d) exhibit the top and the cross-section views of a dual membrane structure, respectively.

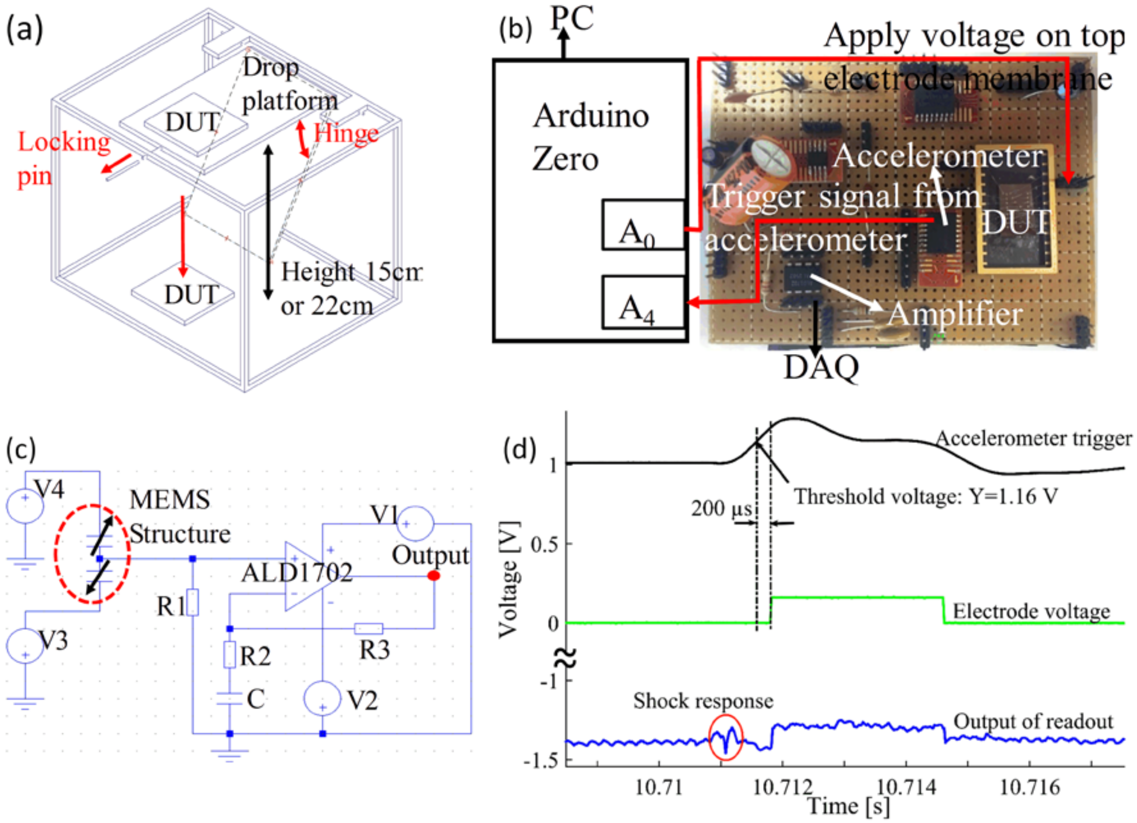

Figure B.2. Experiment Setup: (a) Schematic of drop setup; a pin holds the drop platform and releases it to drop the test board to the hard floor. The adjustable travel distance is set to be 22 cm, corresponding ~ 100 g. (b) Micro-controller board and test board. (c) Simplified schematic of the readout circuit. (d) Temporal profiles of accelerometer, electrode voltage, and output of readout with 100 g shock load.

A custom-made drop test apparatus (Fig. B.2(a)) was constructed to evaluate the shock-mitigated MEMS structures. Four vertical steel pillars support a wooden drop platform with dimensions of 0.6 x 14 x 31 cm at a given height, i.e. 15 cm or 22 cm, from the hard floor. A stopper (small cylindrical wooden pin) pins the platform and when removed, will cause the test board on the platform to drop perpendicular to the floor. Rubber bands were incorporated at the end of the platform, to enhance the rapid drop of the MEMS structures and consequently reduced the friction between the platform and test board. When the test board drops at a given height and hits the floor, the shock load corresponding to the inertia applies to the MEMS structures on board. The fabricated device was mounted in a dual inline package (Spectrum Semiconductor Materials, Inc., HYB02415), and a readout circuit was assembled on custom-made test board as shown in Fig. B.2(b). USB-6210 DAQ from National Instrument collects the resulting data at output of the readout using a sampling frequency of 50 kHz, and MATLAB processes the data using signal analysis with Butterworth digital filter. This filter spans from 500 Hz to 1500 Hz in order to isolate the shock response signal.

Fig. B.2(c) shows the simplified schematic of readout, including a high pass filter with a gain of 21 dB in order to remove low frequency noise. Two variable capacitors model the MEMS structures, followed by a trans-impedance amplifier, including the precision operational amplifier, ALD1702 (Advanced Linear Devices Inc. R1 = 1 MΩ, R2 = 1 kΩ, R3 = 11 kΩ, and C = 1 mF). The readout circuit, a commercial accelerometer (MMA1200KEG, Freescale Inc.), and DUT were all assembled on the test board.

A control was established that the output of the MEMS structures was recorded upon a given shock without applying electrostatic force between the top and bottom membranes. The silicon substrate was biased at -2 V, while maintaining zero voltage difference between the top and bottom membranes. The test board dropped at 22 cm and hit a hard surface, delivering approximately 100 g to the MEMS structures, as measured by the on-board accelerometer. To evaluate the effectiveness of the shock mitigation, we collected outputs of MEMS structures upon a shock at different values of electrostatic force, i.e. DC voltage, applied between the top and bottom membranes.

To implement an *in-situ* control of electrostatic force, a microcontroller and an accelerometer were used to control the timing of electrostatic force upon a shock. When the output of accelerometer exceeded a threshold of 1.16 V, the micro-controller sent a command to apply an electrostatic force within the peak shock amplitude period around 500 μsec (200 μsec Fig. B.2(d)). The force was applied between the top and bottom membranes in order to mitigate the shock effect before the bottom membrane reaches its maximum travel distance. Thus, the timing scheme prevented the bottom membrane from hitting the substrate. To evaluate the effectiveness of in-situ control, we dropped the board containing an accelerometer trigger and a microcontroller. The *in-situ* control not only capably implemented electrostatically mitigation, but also had no influence on the identification of shock response of microstructure in presence of shock impact. Once the microstructure experienced the shock impact, we easily distinguished the shock response in time domain.

To emulate more realistic settings, such as dropping a cell phone with ambient noise, we repeated the above protocol with presence of an acoustic stimulus. We placed a loudspeaker at a distance of 1.6 cm above the DUT to impose an acoustic excitation of 98 dB sound pressure level (SPL) (calibrated by a SPL Meter, CM-130 by Galaxy Audio Company) and performed the drop protocol. The MEMS device along with its readout circuit dropped from the same conditions, and LabVIEW Signal Express visualized the temporal profiles of the accelerometer, the voltage of the top membrane, and readout circuit.

We investigated the responses of MEMS devices under a combination of shock load and electrostatic actuation. MEMS devices typically employ capacitive changes, corresponding to the movement of movable membrane. The performance of shock-mitigated MEMS structures is primarily evaluated by the output voltage of readout circuit, which is proportional to the travel distance of the movable bottom membrane [113]. In theoretical models, the shock is assumed to be a half-sine profile, similar to the shape of an actual shock pulse [112, 114]. Furthermore, the duration of shock load varies from 0.1 to 1 millisecond, which mostly span the duration of the shock pulse for a hard-floor drop test [112].

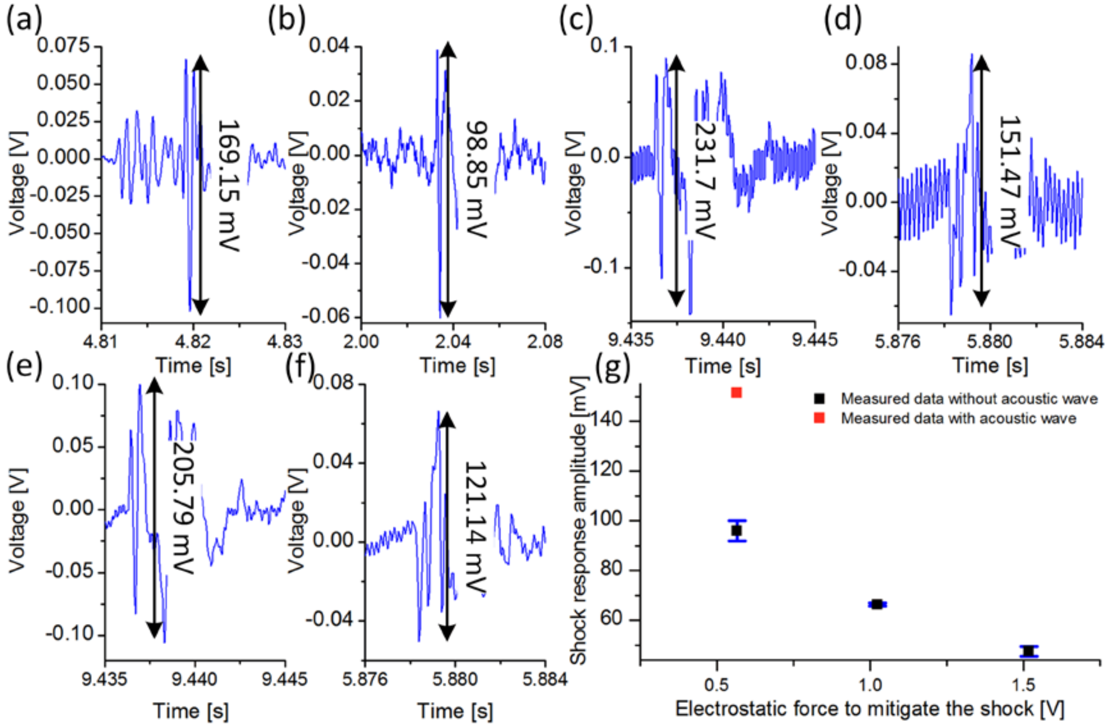

Figure B.3. Ex-situ control of shock-mitigation. (a) Shock response without mitigation. (b) Shock response with mitigation reduced the membrane travel distance by 41.5 % using 0.565 V. (c) Shock response without mitigation in presence of 5 kHz acoustic signal. (d) Shock response with mitigation reduced the membrane travel distance by 34.6 % using 0.565 V in presence of 5 kHz acoustic signal. Output of dual-membrane structure. Shock load 100g and filtered out acoustic stimulus, 5 kHz. (e) without any electrostatic force and (f) with 0.565 V between the top and bottom membranes, respectively. (g) Shock response amplitude as a function of electrostatic force, 0.565 V, 1.023 V, 1.517 V.

MEMS devices responses to shock load can be analyzed either in the time history of the system (time domain approach) or through the shock response spectrum (frequency domain approach) [112]. Fig. B.3(a) and 3(b) depict the temporal profiles of the output of circuit upon external shock of approximately 100 g, (a) without and (b) with electrostatic force between top and bottom membranes. The movable bottom membrane travels towards the substrate due to inertia. By deploying merely 0.565 V between top and bottom membranes, the peak-to-peak amplitude decreases from 169.15 mV to 98.85 mV, resulting in 41.5% reduction. This mitigation method remains effective as well when the microstructure is exposed to both an external shock and an acoustic wave. Fig. B.3(c) and B.3(d) show the microstructure movement generated amplitude of 231.7 mV (c) without any electrostatic force and (d) the amplitude decreases to 151.47 mV, which corresponds to a 34.6% reduction by applying 0.565 V between top and bottom membranes. Higher applied potentials between the top and bottom membrane are also tested under shock, and the resulting peak amplitudes are plotted as a function of applied voltage as shown in Fig. B.3(g). As the electrostatic potential increases, the amplitude of the device decreases.

The electrostatic force between the top and bottom membranes works together with the inherent restoration force of bottom membrane. Electrostatic force is inversely proportional to the effective gap distance and proportional to the effective area of membranes. Inherent restoration force, strongly correlated to the spring constant, is proportional to the thickness of the membranes. However, in practice, the spring constant of thin film is largely dominated by the stress developed inside the thin film. We believe the thin film stress may be responsible for the discrepancies between theoretical estimation and experimental results.

The effectiveness of shock-mitigation can be better illustrated by referring to shock response in frequency domain. Obvious distinction of acoustic wave signal from shock response signal make the data analysis easier. By using a digital filter to filter out the 5kHz acoustic wave signal, the amplitude of shock is decreased from 205.79 mV (Fig. B.3(e) no electrostatic force) to 121.14 mV (Fig. B.3(f) 0.565 V between the two membranes) by 41% reduction, which has a good agreement with the results shown in Fig. B.3(a) and B.3(b). It is concluded that our dual-membrane MEMS structure has capacity to mitigate external shock load effectively under the influence from acoustic wave stimulus, which meets the modeling purpose to be a microphone in cell phone.

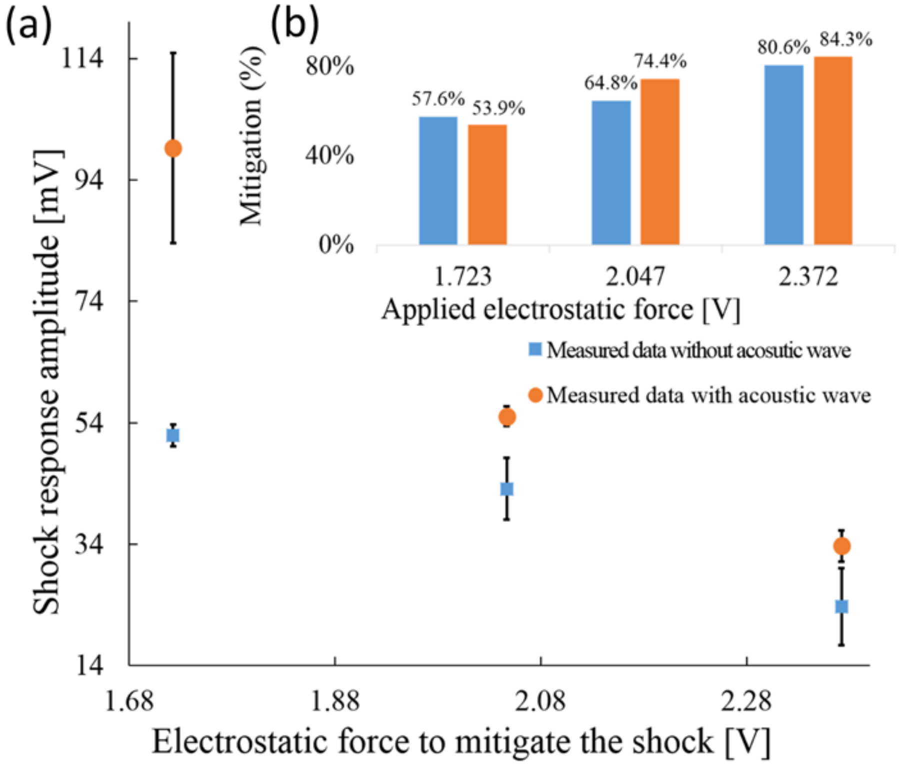

Figure B.4. In-situ control of shock-mitigation: (a) Shock response with different electrostatic force, 1.723 V, 2.047 V, 2.372 V separately. (b) Shock mitigation percentage versus applied electrostatic force between top and bottom membranes.

Similar to the *ex-situ* control, the peak shock amplitude decreases, and the mitigation becomes more effective as the electrostatic force increases. The reduction of shock response with the increasing electrostatic force between top and bottom membranes is shown in Fig. B.4.

We present a shock mitigating technique, using a dual-membrane microstructure, which effectively attenuates the effects of external disturbances such as mechanical shock on a MEMS device. An *in-situ* shock mitigation configuration consists of an accelerometer and shock mitigating controller; the accelerometer senses the shock and triggers the dual membrane structure to apply the electrostatic force to reduce the shock impact. To replicate real life settings, the shock-mitigation method triggers naturally based on conditions measured from the accelerometer and during acoustic excitation on the device. The shock-mitigated method comprises of a simple structure, uses CMOS-compatible materials and manufacturing process, and delivers a highly effective shock mitigation through low voltage electrostatic actuation. This dual membrane MEMS structure improves upon current MEMS devices by providing a shock mitigating profile necessary to maintain the device’s functionality.

APPENDIX C

PHOTO OF THE WIRELESS WEARABLE SENSOR

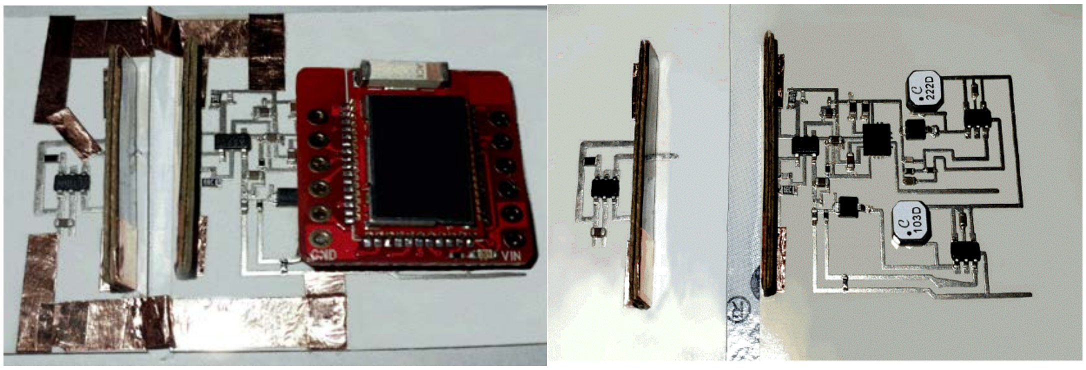

Figure A.1. Photos of the wireless wearable sensor. (a) the wireless wearable sensor on a paper substrate with electronics mounted on. (b) the fully-assembled wireless wearable sensor with the copper-tape bridges connecting and providing power supply to the emitter. BLE Nano2 was mounted on the receiver side to transmit the collected signal to external instrument, such as mobile phone via Bluetooth.

APPENDIX D

ULTRASOUND PRESSURE ATTENUATION WITH INCREASE OF TRAVELLING DISTANCE

In general, overall ultrasound attenuation is characterized by the following exponential decrease of the pressure amplitude p with the travelling distance z:

$$P_1=P_0*e^{-\alpha z}$$

where p0 is the pressure at z=0. The quantify α (expressed in cm-1) is the pressure frequency-dependent attenuation coefficient.

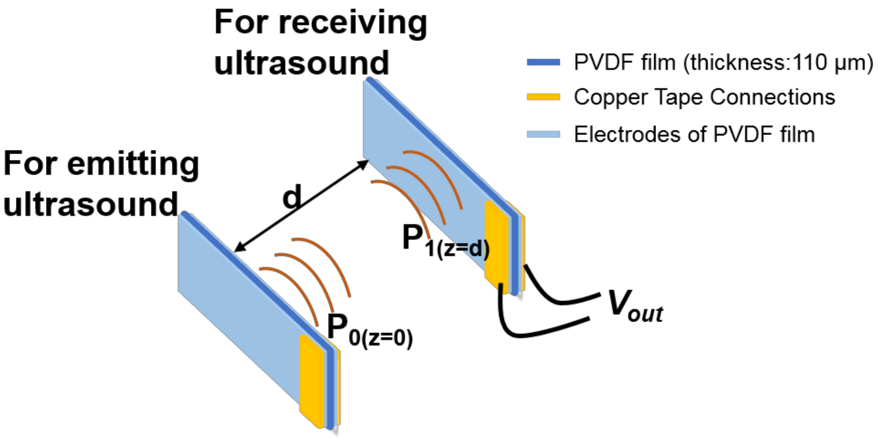

Two PVDF films mounted on the wireless wearable sensor.

One is for emitting ultrasound and the ultrasound pressure is P_0 at zero travelling distance. The ultrasound pressure reaches another PVDF film used to receive attenuated ultrasound, P_1, at a distance of d. The corresponding voltage output V_{out} is corelated to P_1 as a function of d that changes as a function of respiration.

The output voltage generated by the PVDF film is given by:

$$V_{out} = g_{33} \times P_1 \times t$$

where g_{33} ($\frac{V/m}{N/m^2}$) is the piezo stress constant stands for the electric field induced in “3” direction by a stress of 1 Pascal is applied along the “3” axis (thickness mode) and the typical value of PVDF film has $-330\times10^{-3}\,\frac{V/m}{N/m^2}$. t is the thickness of the PVDF film, 110 μm.

APPENDIX E

ALGORITHM OF CUSTOM-MADE MOBILE APP

Packet format:

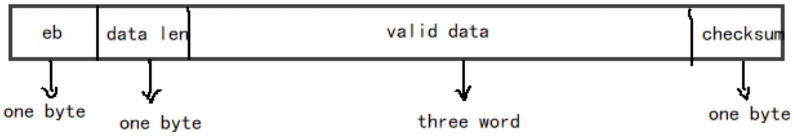

Android Application Signal Processing Algorithm

```
Init: data ← data from sensor                    //save bitstream data sent in 16 binary system.
Init: package_len ← length of effective data;  data_mv ← save valid data;  data_time ← save sample time
      size ← record the number of packets;  length ← the number of packets processed currently
while length<size do
    Check: Check the head of packet must be ‘0xeb’
    Through Butterworth filter:
            Init: az bz ← read filter coefficients from ‘butter_coe.text’    //Coefficients file created in MATLAB
            data_first ← save the filtered data
    Deal: $data\_first(t)=bz_0*data\_mv(t) + bz_1*data\_mv(t-1) + ... + bz_{order}*data\_mv(t-order) – az_1*data\_first(t-1) – az_2*data\_first(t-2) - ... -az_{order}*data\_first(t-order)$    //order ← filter order
            Init: deal_dis ← save transition data;  data_second ← save second processed data (represents slope)
            Second Deal:
            $deal\_dis(t) ← ln(|1-(data\_first(t).\text{^}2)/(Amplitude\_Level\text{^}2)|)/(-a)$;
    $data\_second(t) ← (deal\_dis(t-1) - deal\_dis(t))/(data\_time(t)-data\_time(t-1))$
Calculate FEV1 and FEV1/FVC:
    Init: max_Data ← maximum of filtered data with t>0.5s;  max_Time ← the time of max_Data;
          min_Time ← the time of trough value before maximum data;
          delta_Time ← x-intercept of maximum slope plus one;  time_Plus ← truly effective intersection
```

```
            Deal: for t in [data_second.size()-pakage_len/2, data_second.size()] do
        if (max_data<data_second(t)) max_data ← data_second(t)
                              max_time ← t
    end of for
    for t<max_Time do
        if(data_first(t)>data_first.get(t-1))
            t--;
    end of for
    min_time ← t
    for t in [min_Time, max_Time] do
      Find the maximum slope point.
    end of for
    delta_Time ← 1+ x-intercept of maximum slope
                      Time_Plus ← closest valid point to delta_Time
            FEV1 ← time_Plus
  FEV1/FVC ← FEV1/max_Data
end of while
Show: display waveform.
```

APPENDIX F

SPIROMETER VS. THE WIRELESS WEARABLE SENSOR: EXPERIMENTAL RESULTS OF A SUB-OPTIMAL RESPIRATION

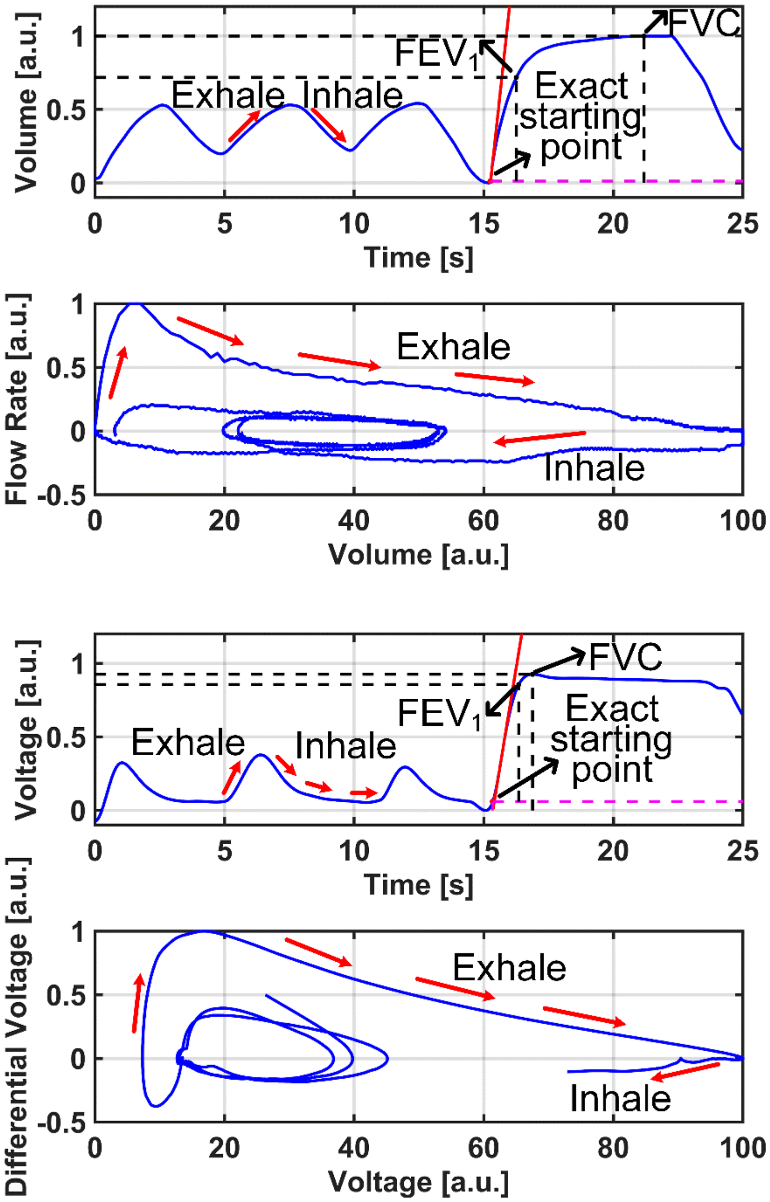

Figure D.1. Respiratory behavior of spirometer (a) Volume-time tracing, (b) Flow rate vs. volume and that of the wireless wearable sensor (c) Voltage-time tracing, (d) Differential voltage vs. maximum achieved voltage, respectively.

In results from both the spirometer in Fig.S-3(b) and the wireless wearable sensor in Fig.S-3(d), a concave tracing was observed representing the respiratory behavior of the specific test on the volunteer is sub-optimal. For the results displayed in the figures, the

FEV_1/FVC ratios of 71% and 72.5% were achieved by spirometer and the sensor during the attempt, respectively, which confirms the sub-optimal respiratory performance of this volunteer was detected by both spirometer and the sensor. When the FEV_1/FVC ratio is smaller than the pre-set value in the custom-made app (75%), an alerting message will display on the screen of the mobile phone.

APPENDIX G

CUSTOM-MADE SOFTWARE FOR DATA COLLECTION

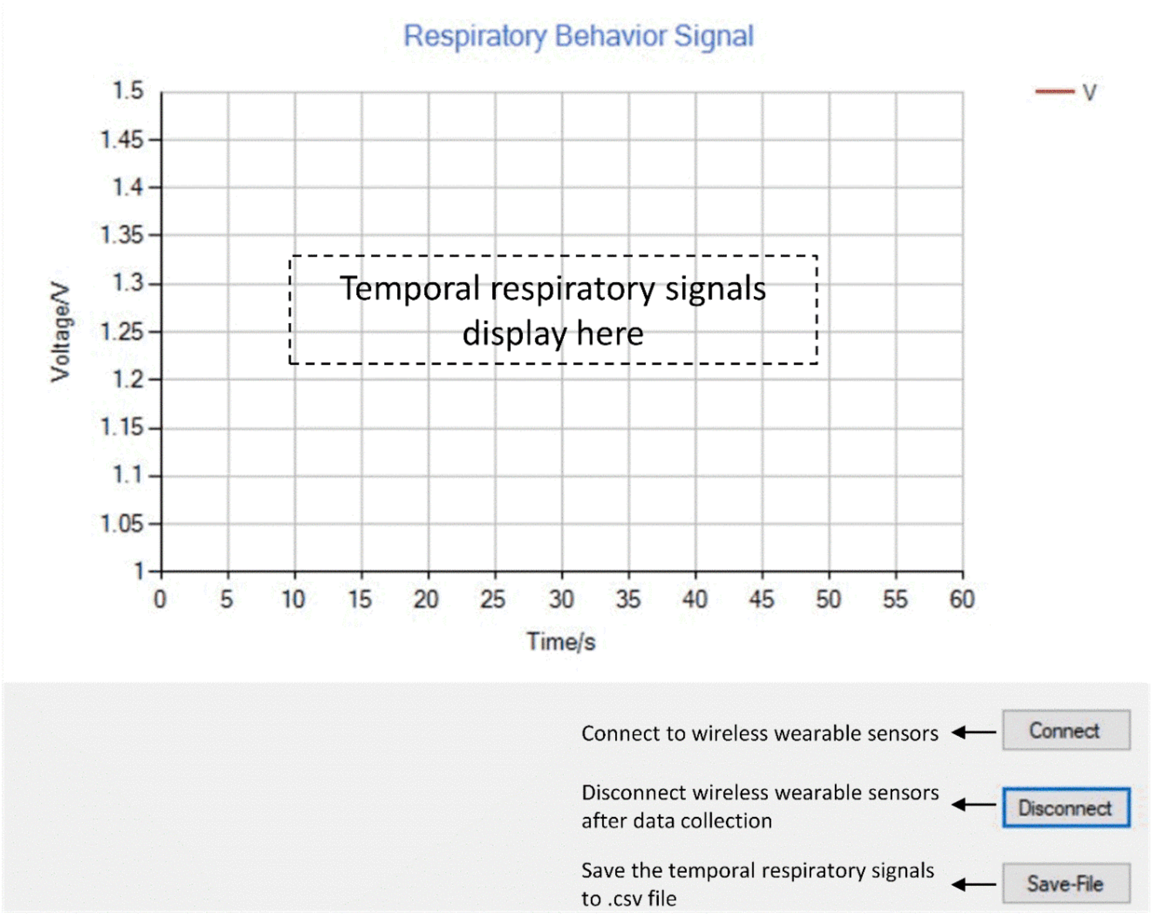

Temporal respiratory signals display here

Connect to wireless wearable sensors

Disconnect wireless wearable sensors after data collection

Save the temporal respiratory signals to .csv file

Figure E.1. The interface of custom-made software installed in a laptop for data collection. “Connect” button for connecting the wireless wearable sensors to a laptop via Bluetooth, “Save-File” for saving the temporal respiratory signals displayed as .csv files “Disconnect” button for disconnecting the wireless wearable sensors.

APPENDIX H

SCHEMATIC OF WIRELESS WEARABLE SENSOR

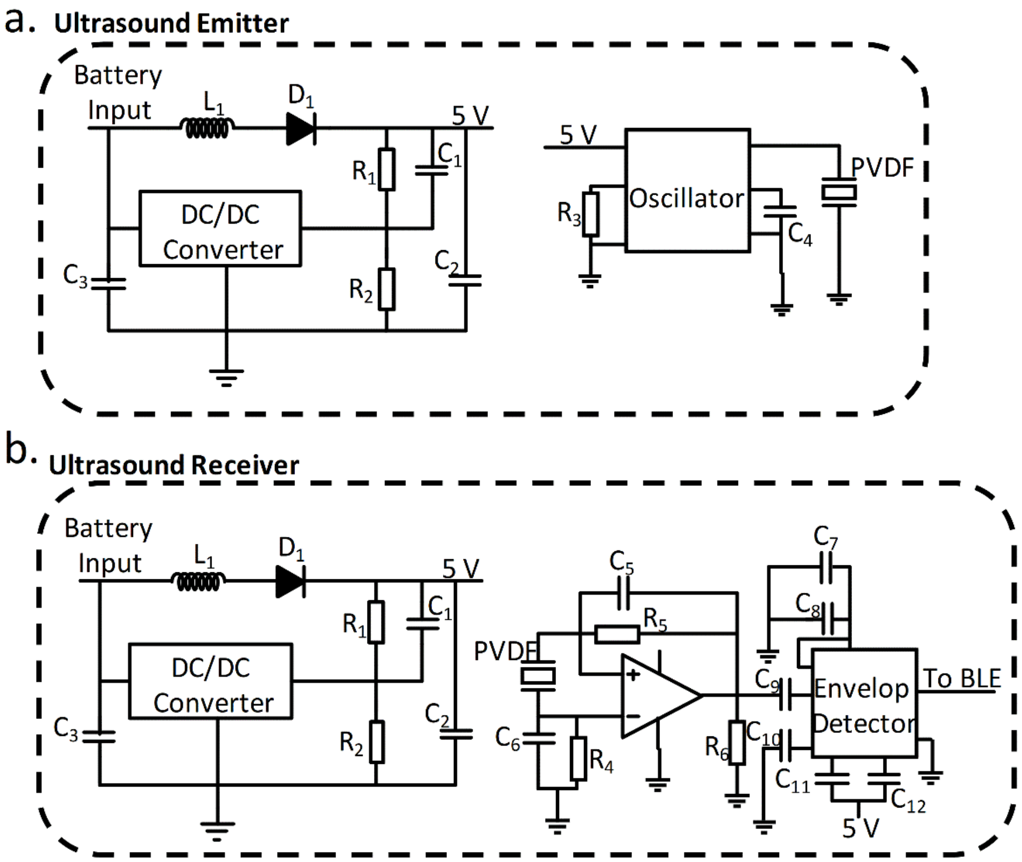

Figure

Figure F.1. The circuit diaphragm of the wireless wearable sensor. (a) The circuit of ultrasound emitter. A DC/DC converter steps up 3.7 V of lithium battery to 5V, providing adequate power to a voltage-controlled oscillator for generating a 50 kHz ultrasound via PVDF film. (b) The circuit of the ultrasound receiver. A DC/DC converter boosts the 3.7 V of lithium battery to 5V to power corresponding modules, an op-amp to amplify the received modulated signal, and an envelope detector to extract the respiratory behaviors for wireless transmission via an onboard antenna in BLE module.

APPENDIX I

GAUSSIAN WEIGHTED MOVING AVERAGE SMOOTHING

Gaussian smoothing is a traditional linear smoothing. It can accentuate the features after convolution with studied signals that have similar center-peaked features[125]. Respiratory behaviors, including respiratory rates, are individual-dependent and characterized by center-peaked profiles. For eleven subjects in this study, experimental respiratory rates are variable within a range of 0.19 to 0.34 Hz. In order to make the inspiration and expiration, corresponding to the decrease and increase in the output signals more prominent, we applied the gaussian-weighted moving average smoothing window (MATLAB) based on each respiratory rate per subject. The window size is calculated as follows:

$$\text{window size} = \left\lceil \mathrm{f_s} \times \frac{1}{\mathrm{f_{subject}}} \right\rceil$$

$\mathrm{f_s}$: sampling frequency of the respiratory signal, 10 Hz

$\mathrm{f_{subject}}$: respiratory rate of each subject

$\lceil\ \rceil$: ceiling function, a function that maps the result to the least integer greater than or equal to the result

APPENDIX J

RESPIRATORY FEATURES USED IN RANDOM FOREST CLASSIFIERS

Random forest classifiers classify the postures based on the respiratory features, including filtered respiratory data themselves, the first and second differential of the data, mean and variance, and the wavelet coefficients.

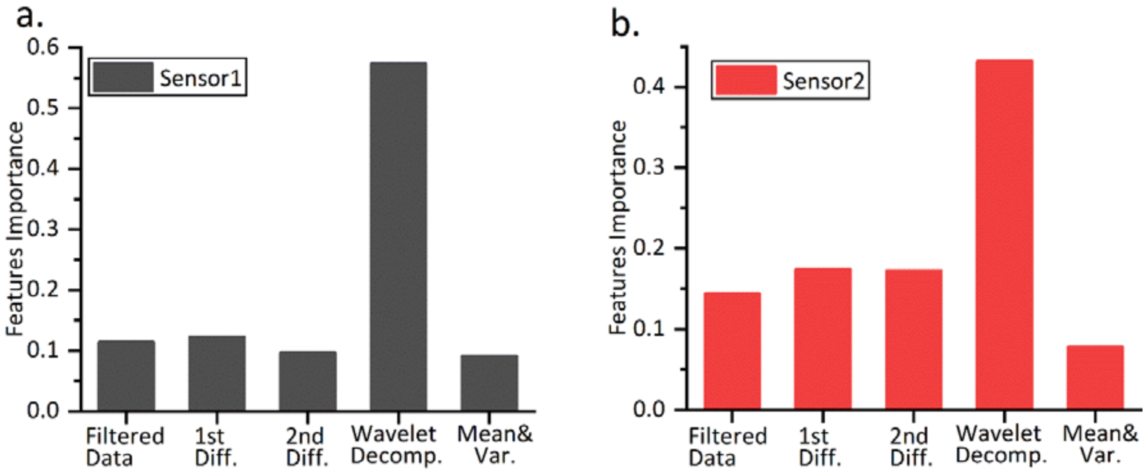

Figure H.1. Feature importance rankings of Sensor1 (abdominal respiration) and Sensor2 (chest respiration).

(a) Five respiratory features were extracted and fed in random forest classifiers. The wavelet decomposition consistently contributes primarily in final prediction accuracies, as the same in (b). Mean and variance can present the respiratory profiles in the temporal domain, first and second differentials correlate to the mobility of respiratory muscles, the higher mobility associates with more significant inspiratory and expiratory ability, providing a parameter of healthy lung function.

The contribution of wavelet decomposition in final prediction accuracies is prominent and consistent in Sensor1(Abdominal respiration, Figure S4a), Sensor2 (Chest respiration, Figure S4b), and Sensor1&Sensor2(Abdominal and Chest respiration, Figure 4C). Despite the wavelet decomposition, random forest classifiers also used first and second differentials, which are chest wall mobility-related features. Chest wall mobility was correlated with respiratory muscle strength and lung function. Higher chest wall mobility was associated with more significant maximum inspiratory and expiratory pressures, forced vital capacity, and inspiratory capacity[126], which can be determined from the collected respiratory data using the first and the second differentials. The first and second differentials represent the speed and the acceleration of contraction and expansion of the chest and abdominal walls, providing a reference for strength and lung function. Filtered respiratory signals and corresponding mean and variance can present more details of respiratory profiles in the temporal domain.

APPENDIX K

GENERIC CLASSIFIER WITH MORE SUBJECTS

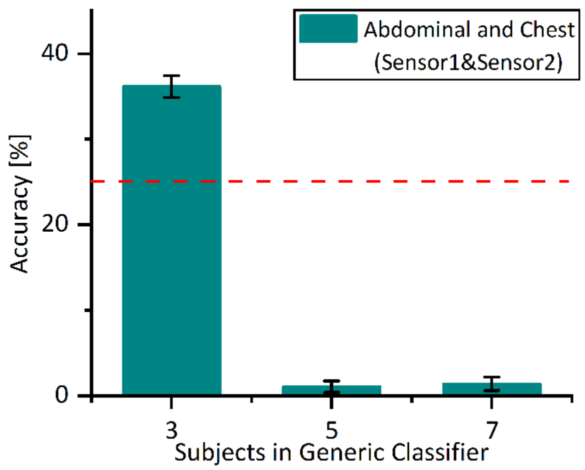

Figure I.1. Generic classifier with increasing subjects. With the number of subjects included more in a generic classifier extracting respiratory features from abdominal and chest respiration, the prediction accuracies become worse, 36.12±1.28%, 1.04±0.68%, 1.38±0.81%, respectively. The prediction accuracies of the generic classifier with five, and seven subjects are even lower than the random probability 25%, showing the generic model has poor ability to extract the features of respiratory behaviors.

APPENDIX L

WEIGHTED-ADAPTIVE CLASSIFIER WEIGHT DISTRIBUTION

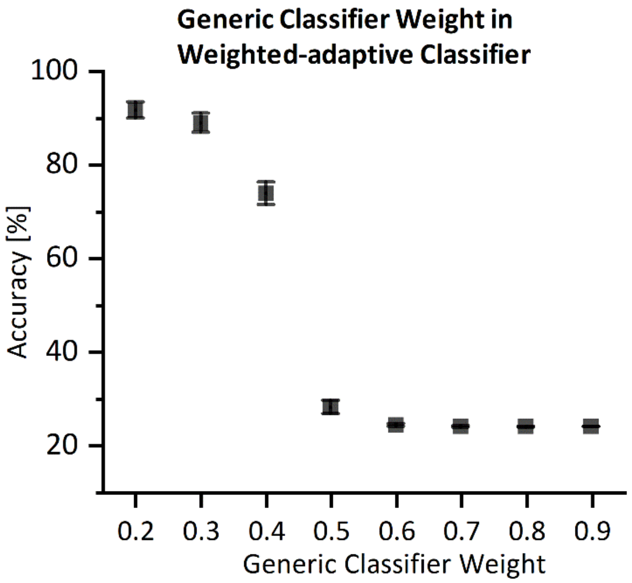

Figure J.1. Weights of generic and individual classifiers in weighted-adaptive classifier. With the increase of weight of generic classifier, starting from 0.2 to 0.9, in weighted-adaptive classifier, the prediction accuracy decreases. When the weight of generic classifier equals to 0.2, the prediction accuracy mark highest accuracy, the corresponding weight of individual classifier is 0.8. Therefore, experimentally weighted-adaptive classifier is a weighted probability of 0.8 probability from the individual classifier and 0.2 probability from the generic classifier.